

AN INVESTIGATION OF THE FEASIBILITY
OF UTILIZING A NEGATIVE CONTROL GRID
IN A CROSSED-FIELD ELECTRON GUN

By
FURNIE SMITH BRYANT, JR.

A DISSERTATION PRESENTED TO THE GRADUATE COUNCIL OF
THE UNIVERSITY OF FLORIDA
IN PARTIAL FULFILLMENT OF THE REQUIREMENTS FOR THE
DEGREE OF DOCTOR OF PHILOSOPHY

UNIVERSITY OF FLORIDA

August, 1966



© Furnie Smith Brvant, Jr. 1968

ALL RIGHTS RESERVED

ACKNOWLEDGMENT

The author wishes to acknowledge the assistance provided by his chairman, Dr. A. D. Sutherland, and the members of his supervisory committee throughout the entire program of graduate study, with a very special expression of gratitude to Dr. Sutherland, without whose faith and guidance this dissertation would not have been possible.

A special acknowledgment to the Sperry Electronic Tube Division, Gainesville, Florida, where the author was employed during the course of graduate study, for sponsoring the project and granting permission for use of the material for this dissertation. The author also wishes to express his gratitude for the generous assistance provided by Sperry's advanced education program.

The author wishes to thank Mr. Fred Hansen for his assistance in taking and reproducing the movies and photographs.

TABLE OF CONTENTS

| | Page |
|---|------|
| ACKNOWLEDGMENTS | 11 |
| LIST OF TABLES | v |
| LIST OF FIGURES | vi |
| KEY TO SYMBOLS | x |
| ABSTRACT | xi |
| INTRODUCTION | 1 |
| CHAPTER | |
| I. ELECTRON GUN CLASSIFICATION, BASIC PROBLEM AND GENERAL APPROACH | 4 |
| II. TECHNICAL DISCUSSION | 11 |
| III. EXPERIMENTAL EVALUATION | 45 |
| IV. CONCLUSIONS | 81 |
| APPENDICES | |
| A. PROTOTYPE MAGNETRON-INJECTION GUN DIODE DESIGN | 84 |
| B. DESIGN OF EXPERIMENTAL GRID STRUCTURES .. | 92 |

Table of Contents (Continued)

| | Page |
|--|------|
| APPENDICES | |
| C. DERIVATION OF THE ELECTROSTATIC POTENTIAL DISTRIBUTION FOR AN ARRAY OF LINE CHARGES LOCATED INSIDE A CYLINDRICAL CONDUCTING BOUNDARY | 100 |
| LIST OF REFERENCES | 109 |
| BIOGRAPHICAL SKETCH | 112 |

LIST OF TABLES

| Table | | Page |
|-------|---|------|
| 1a. | A Summary of Magnetron-injection Gun Design Values for the Experi- mental Prototype Diode | 49 |
| 1b. | A Summary of Prototype Diode Operation | 53 |
| 2. | A Summary of the 24 Vane Grid Structure Test Data | 59 |
| 3. | A Summary of the 24 Vane Grid Structure Transfer Characteristic Data . | 62 |
| 4. | Calculated Versus Measured Beam Size . . | 65 |
| 5. | A Summary of the Helical Grid Structure Test Data | 68 |
| 6. | A Summary of the Helical Grid Structure Transfer Characteristic Data . | 70 |
| 7a. | Tube Parameters | 78 |
| 7b. | Typical Beam Parameters | 78 |

LIST OF FIGURES

| Figure | | Page |
|--------|--|------|
| 1. | Typical Electron Trajectories for a Cylindrical Diode and Triode | 9 |
| 2. | Typical Electron Trajectories for a Cylindrical Diode and Triode in the Presence of both Axial Magnetic and Radial Electric Fields | 9 |
| 3. | Cross-section of a Typical Magnetron-injection Gun | 12 |
| 4. | Typical Grid Structure | 14 |
| 5. | Typical Electron Trajectories for a Truncated Magnetron-injection Gun . . . | 16 |
| 6. | Projection of an Emitting Strip onto the $r - \theta$ Plane | 19 |
| 7. | Projection of Non-emitting Strip from a Conical Cathode onto the $r - \theta$ Plane | 19 |
| 8. | Beam Projection onto $r - \theta$ Plane for an Infinitely Strong Axial Magnetic Field | 22 |
| 9. | Concentric Ring Grid Structure | 22 |
| 10. | Conical Parallel Wire Grid and Projection | 23 |
| 11. | Typical Electron Movement About the Cathode of a Crossed-field Gun | 26 |

List of Figures (continued)

| Figure | | Page |
|--------|---|------|
| 12a. | Planar Model of Parallel Vane Grid . . | 28 |
| 12b. | Single Cell of Symmetry | 28 |
| 13. | Equipotential Contour Comparison of Cylindrical Diode and Triode | 32 |
| 14. | Comparisons of Cathode Current Den- sity Distribution (Ref. Fig. 12) | 34 |
| 15. | Computed Trajectories with Space- charge in the absence of Magnetic Field | 35 |
| 16. | Equipotential Contours with Space- charge (% lines refer to anode voltage) | 38 |
| 17. | Equipotential Contours without Space- charge (% lines refer to anode voltage) | 39 |
| 18. | Cross-sectional view of Beam Tester. . | 46 |
| 19. | Photograph of Beam Tester. | 47 |
| 20. | Plot of Magnetic Field used in Beam Analysis | 51 |
| 21. | Prototype Diode Microperveance versus $B/\sqrt{V_a}$ ratio | 54 |
| 22. | Beam Profile for the Prototype Diode with Magnetic Field Parameter $B/\sqrt{V_a}$ set at a) 17.1 , b) 19.8 , c) 22.7 , d) 27.7 | 55 |
| 23a. | Vane Grid Structure | 57 |
| 23b. | Component Gun Parts | 57 |
| 24. | Completely Assembled Vane Grid Gun . . | 58 |

List of Figures (continued)

| Figure | | Page |
|--------|---|------|
| 25. | Microperveance and Anode Current versus $B/\sqrt{V_a}$ ratio for the Vane Grid Structure | 60 |
| 26. | Grid Transfer Characteristics for the Vane Grid Structure | 63 |
| 27a. | Photograph of Helical Grid Structure | 67 |
| 27b. | Photograph of Beam Profile for Helical Grid Structure. | 67 |
| 28. | Microperveance and Anode Current versus $B/\sqrt{V_a}$ Ratio for the Helical Grid | 69 |
| 29. | Transfer Characteristics for the Helical Grid | 71 |
| 30. | Beamlet Pattern Produced by the Vane Grid Structure , | 74 |
| 31a. | Typical Precession of a Single Beam- let (Complete Beam Contains 24 Beamlets) | 75 |
| 31b. | Plot of Precession versus Axial Distance (Vane Grid Structure). | 75 |
| 32. | Photograph of Beam Current, Grid Voltage and Grid Current | 77 |
| 33. | Plot of Efficiency versus Frequency for L-band Tube (Vane Grid Structure.) . | 80 |
| A-1. | Cross-section of Truncated Magnetron- injection Gun showing Prototype Diode Design Values | 87 |

List of Figures (continued)

| Figure | | Page |
|--------|---|------|
| A-2. | Normalized Potential ϕ versus z with Electron Emission Profile Shown for Prototype Diode | 89 |
| B-1. | Single Cell Electrolytic Tank Equipotential Plot | 94 |
| B-2. | Equipotential Profile at Cut-off . . . | 95 |
| B-3. | Cross-section of a 24 Vane Grid Structure | 96 |
| B-4. | Helical Grid Structure | 99 |
| C-1. | Sequence of Reducing a Line Charge Located off Axis to Standard Form . . . | 101 |
| C-2. | Conformal Transformation | 103 |

KEY TO SYMBOLS

| Symbol | Description |
|--------------|--|
| a | Helix radius |
| b | Velocity parameter |
| B | Increasing wave parameter |
| B_z | Axial magnetic field |
| c | Gain parameter |
| e | Electron charge |
| E | Electric field intensity |
| ϵ_0 | Dielectric constant of free space |
| γ | Radial phase constant |
| I | Beam current |
| I_a | Anode current |
| J_0 | Current density at r_0 |
| λ_e | Electronic wave length |
| K | Perveance |
| m | Electron mass |
| η | Magnitude of electron charge-to-mass ratio |

Key to Symbols (continued)

| Symbol | Description |
|----------------|---|
| Q | Space-charge parameter |
| q_l | Line charge |
| r | Radius |
| r_c | Cathode radius |
| r_o | Spherical radius of conical cathode magnetron-injection gun |
| $\dot{\theta}$ | Angular velocity radians/sec. |
| V_o | Voltage to which electrons are accelerated |
| V_a | Anode voltage |
| Z | Interaction impedance |
| $L \]$ | Numbers enclosed denote author references |

Abstract of Dissertation Presented to the Graduate Council
in Partial Fulfillment of the Requirements for the Degree of
Doctor of Philosophy

AN INVESTIGATION OF THE
FEASIBILITY OF UTILIZING A NEGATIVE
CONTROL GRID IN A CROSSED-FIELD ELECTRON GUN

By

Furnie Smith Bryant, Jr.

August, 1966

Chairman: Dr. Alan D. Sutherland

Major Department: Electrical Engineering

The purpose of this research program was to investigate the feasibility of utilizing a negative, non-intercepting, control grid in a crossed-field electron gun. A further objective was to establish design criteria and procedures for those grid structures where feasibility was established.

Theoretical and experimental aspects of the application of a negative non-intercepting control grid to a

magnetron-injection gun are discussed. Several grid structures are analyzed in terms of perveance reduction factor and grid transfer characteristics.

Several experimental guns were designed and evaluated. Perveances in excess of 12×10^{-6} amp/volt^{3/2}, for a grid Mu in excess of 6 for absolute cut-off, were observed. Experimental results of beam tester work are presented in the form of both photographs and data evaluation of beam patterns as observed on a moving carbon target. An electron gun utilizing this principle was successfully employed in an L-band traveling wave tube and tests on that tube are described.

INTRODUCTION

Present use of microwave amplifier tubes in pulsed doppler radar has necessitated both a high duty cycle and high repetition rate capability. A control electrode, such as a negative grid, offers many advantages to the user of the amplifier. Beam switching by anode modulation requires a large voltage swing; and, consequently, excessive modulator power is dissipated in charging and discharging the anode electrode capacity. A substantial modulator power reduction can be achieved by utilizing a negative control grid. Positive control grids which intercept current are restricted to medium power tubes--the limit being dictated by the average grid power dissipation capability and/or the emission of secondary electrons. This restriction is removed in the negative grid case because the grid does not intercept current.

Grid designs for both positive and negative grid operation have been utilized in Pierce-type [1] electron guns for several years; however, to the author's know-

ledge, these principles have not been extended to the crossed-field gun--in particular magnetron-injection guns.

Basically, grid control methods are of two types: intercepting and non-intercepting. Non-intercepting grids operate on the principle of electron emission suppression beneath the grid during on-time. This is accomplished in the positive control grid by either selective cathode coating or cathode shadowing. Alternatively, with negative control grids, the potential of the control grid never exceeds that of the cathode; therefore, the force due to electric fields between the grid and cathode is such as to repel electrons, and suppression is inherent. Associated with the addition of a negative control grid is a substantial reduction of perveance even for medium μ (15 - 30) operation. Perveances for aperture anode, negative grid, Pierce-type electron guns are limited to values in the order of 1×10^{-6} amp/volt^{3/2} for absolute cut-off μ 's of 30 - 50.¹ In addition, even at the lower values of grid μ and perveance, there is an undesirable current density variation across the cathode surface due to electric

¹These limits were reported by Ashley, Sutherland and Kolb [2].

field suppression by the grid.

The extension of the negative grid concept to the (linear beam) crossed-field class of electron guns offers two definite advantages. First, the cathode-to-beam area convergence for the conventional hollow beam gun is unity. This places an upper limit on beam current density. In the crossed-field magnetron-injection gun, this limit is increased because the area convergence is inversely proportional to the cathode cone semiangle which is typically very small. Second, the perveance for the basic diode magnetron-injection gun greatly exceeds that of the conventional planar design. This increased perveance capability permits an increase in bandwidth capability since the two are proportional.

The aim of the research about which this dissertation is concerned was to explore the feasibility of incorporating the negative control grid feature in magnetron-injection guns, and to determine factors limiting the design of such guns.

CHAPTER I

ELECTRON GUN CLASSIFICATION, BASIC PROBLEM AND GENERAL APPROACH

Electron Gun Classification

Typically, electron guns are classified in terms of their perveance--a parameter which remains invariant when the gun is scaled. Electron gun perveance, K , is defined for a diode gun by

$$K = I/V^{3/2} \quad (1)$$

where

I = the cathode current in amperes

V = the anode voltage in volts

An electron gun is referred to as having a high perveance if it is an order of magnitude greater than unity microperveance.¹ Similarly, a low perveance electron gun is

¹Since typical gun perveances are on the order of 10^{-6} it is customary to use the term microperveance which is the perveance defined by Equation (1) multiplied by 10^6 .

one with a microperveance an order of magnitude below unity. In addition to classification by perveance, guns are referred to in accordance with their geometric configuration; for example: planar, Pierce-type and crossed-field. For the first two types, the electrons flow from the cathode to anode along trajectories that do not cross magnetic lines of flux; therefore, these guns do not depend on a magnetic field for proper operation. However, the third type, the crossed-field gun, does require a magnetic field. With the latter, there are two classes or types: (1) guns in which the magnetic field is perpendicular to both the electric field and the direction of beam propagation and, (2) those in which the magnetic field is parallel with the direction of beam propagation. Magnetron-injection guns fall into this second category of crossed-field guns.

The design method for the Pierce-type electron gun differs radically from the crossed-field gun; therefore, the negative grid design procedures are similar in concept, but not the same. Prior to 1960, the only analytic space-charge flow solutions used in the art of electron gun design for microwave tubes were those for rectilinear flow between two planes, two cylinders or two spheres.

In 1958, Kirstein and Kino [3] published a basic contribution to the theory of curvilinear space-charge flow, which led to radical departure from the limitations imposed by the rectilinear flows which had formed the basis for electron gun design up to that point. This was followed by a sequence of papers by Kirstein [4], Waters [5], [6] and Dryden [7], [8] leading to the synthesis of space-charge flow pattern suitable for the design of magnetron-injection guns. Harker [9], [10] in the same period, published analytic methods for determining the requisite electrode shapes for setting up and supporting such flows. In addition, Kino and Taylor [11] have published solutions using planar, rather than axially symmetric geometries. More recently, Okoshi [12] published an improvement of the Kino-Taylor theory to account approximately for centrifugal forces. The computer methods developed by Dryden [7] were used in the present investigation for the design of the prototype diode magnetron-injection guns.¹

¹The term prototype diode is defined as the diode electron gun, consisting of cathode, focus electrode, and anode, which would result if the negative grid were physically removed from the triode.

Basic Problem

By definition, the path of an electron will be referred to as "normal" if its trajectory is that of the prototype diode to which a grid is added. The placement of a grid in the cathode-anode region will cause beam interception and/or deflection. To illustrate this, consider the cylindrical diode. Figure 1a shows the paths of electron flight from the cathode to anode in the absence of magnetic field. These trajectories are radial as the only electric field component present is radial. Figure 1b shows the effect of adding a negative grid. The grid is seen to cause a focusing action which destroys the laminar¹ diode flow. The grid apertures act as convergent electrostatic lenses, imparting lateral motion to all electrons except those emitted at a plane of symmetry between two wires.

When an axially symmetric field is placed parallel to the cathode axis, the problem of beam ^{disturbance} perturbation caused by the grid takes on additional complexity. In

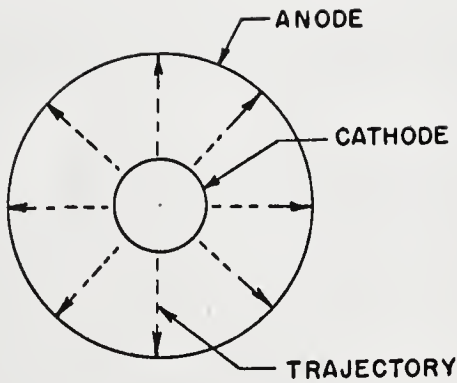
¹ Laminar flow means that the electron velocity function is a single valued function of position, and that the beam can be divided by imaginary surfaces into isolated non-penetrating sections.

the absence of the grid, for the cylindrical diode case just discussed, the trajectories are bent as depicted in Figure 2a. The addition of the grid causes transverse deflections of the electron paths to be superimposed upon this basic flow pattern. The resultant non-laminar curvilinear flow becomes so complex as to make an analysis, which includes the all important effects of space-charge, well nigh impossible. This is illustrated in Figure 2b.

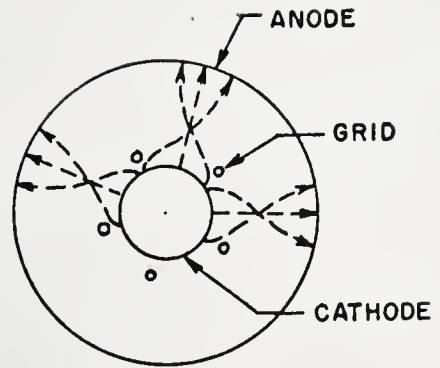
While the cylindrical diode, and triode, have been utilized in the above to illustrate this point, the flow in the magnetron-injection gun is even more complex. In such guns, an axial electric field component is purposely introduced, for example, by forming the anode and cathode as portions of concentric conic sections. This is done so as to provide an axial acceleration component which causes the electrons to turn and eject from the gun without striking the anode, when the magnetic field is present. This non-laminar three dimensional motion makes analytical methods of predicting the space-charge flow patterns hopelessly complicated.

General Approach

For the reasons just outlined, the procedure used in this investigation is largely experimental. The

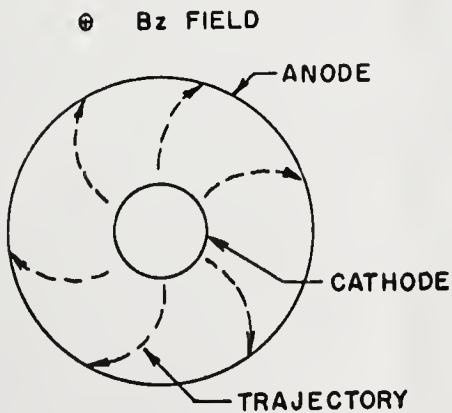


1a. Diode

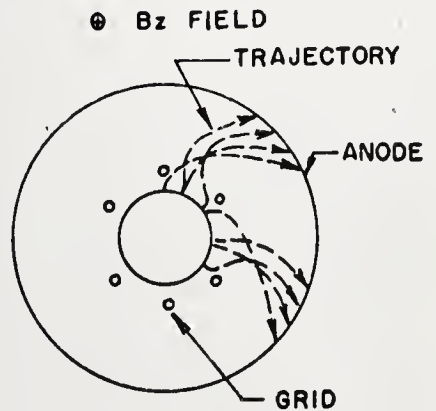


1b. Triode

Figure 1. Typical Electron Trajectories for a Cylindrical Diode and Triode



2a. Diode



2b. Triode

Figure 2. Typical Electron Trajectories for a Cylindrical Diode and Triode in the Presence of both Axial Magnetic and Radial Electric Fields

prototype diode version of the magnetron-injection gun utilized was designed using the analytic methods of Dryden and Harker referred to above. Various grid structures were then added, and the resultant performance was then experimentally determined. Where feasible, approximate analytic methods were then developed to explain the observed experimental performance.

CHAPTER II

TECHNICAL DISCUSSION

Introduction

A cross-sectional view of a magnetron-injection gun is shown in Figure 3. The component parts are as labeled. The theory of operation is best described by considering a single electron emitted from any point on the cathode. In the cathode anode region the electric field will have components both parallel and perpendicular to the cathode surface. Therefore, as the electron leaves the cathode, it will experience both radial and axial accelerations. The radial acceleration vector is perpendicular to the axial magnetic field. The resultant Lorentz force will cause the electron trajectory to bend around the cathode. A condition of balanced flow will occur when the centrifugal force, electric field force and magnetic field force are equal. The presence of the axial component of electric field causes electron ejection from the gun. When

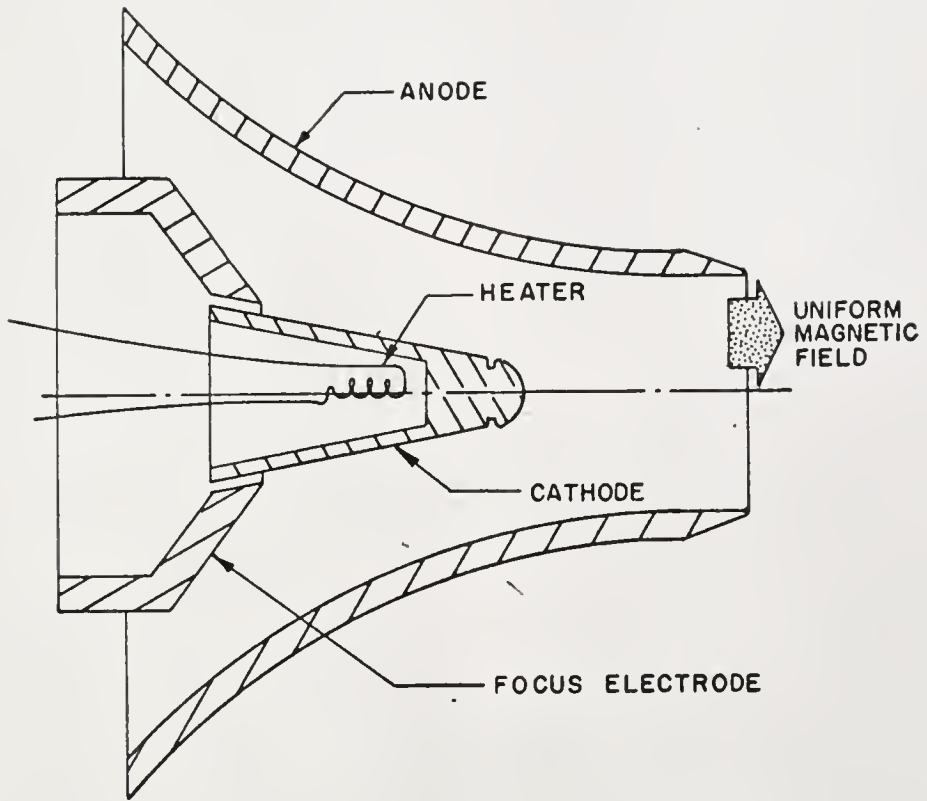


Figure 3. Cross-section of a Typical Magnetron-injection Gun

properly designed, in the presence of space-charge, all other electron trajectories will be magnifications of this one. The anode of the magnetron-injection gun, unlike the cylindrical diode, is non-intercepting. The beam is ejected from the gun into a drift region. If the cathode is truncated, the beam will be hollow; thus, the often used term hollow beam magnetron-injection gun.

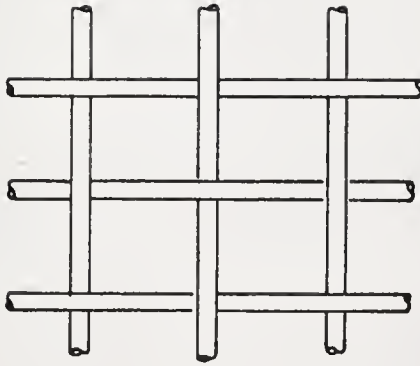
The object is to select an appropriate grid configuration that offers a minimum perturbation to the normal electron flow pattern.

Factors Effecting the Selection of a Grid Configuration

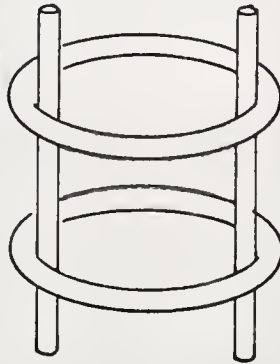
Beam Dynamics

The first decision required is the establishment of a grid configuration which least affects the electron dynamics of the prototype electron beam. Figure 4 shows three grid configurations often used in cylindrical triodes. For the Pierce and planar triode guns, the mesh grid is usually selected. The supported parallel grid ring and helical grid are more appropriate for the conical triode gun.

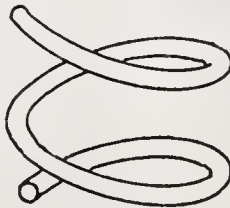
Some insight into the grid selection for a crossed-field negative grid gun can be gained from examining



4a. Mesh Wire Grid



4b. Supported Parallel
Grid Ring



4c. Helical Grid

Figure 4. Typical Grid Structure

Equation (2). This equation is known as Busch's theorem and shows that the angular velocity of a charged particle moving in a static, axially symmetric, magnetic field is a function of position only.

$$\dot{\theta} = \frac{\eta B_z}{2} \left(1 - \frac{r_c^2}{r^2} \right) \quad (2)$$

In this equation r_c refers to the radial coordinate of the point of electron emission from the cathode and r is the radius anytime later. A typical plot of the trajectory in the $r - z$ plane for an electron emitted from the center section of the cathode would be as shown by the solid line in Figure 5. Dryden [7] shows that all other trajectories are simply magnifications of these. Therefore, electrons originating from the ends of the cathode would appear as illustrated by the dotted trajectories. The grid selection must permit electron passage over several grid sections in the gun region as radial expansion, inherent in the gun operation, produces an angular velocity in accordance with Busch's theorem.

If electrons from a thin strip along the cathode are tagged and identified with respect to the particular area location from which they were emitted (independent of the time of emission), their projection onto the $r - \theta$

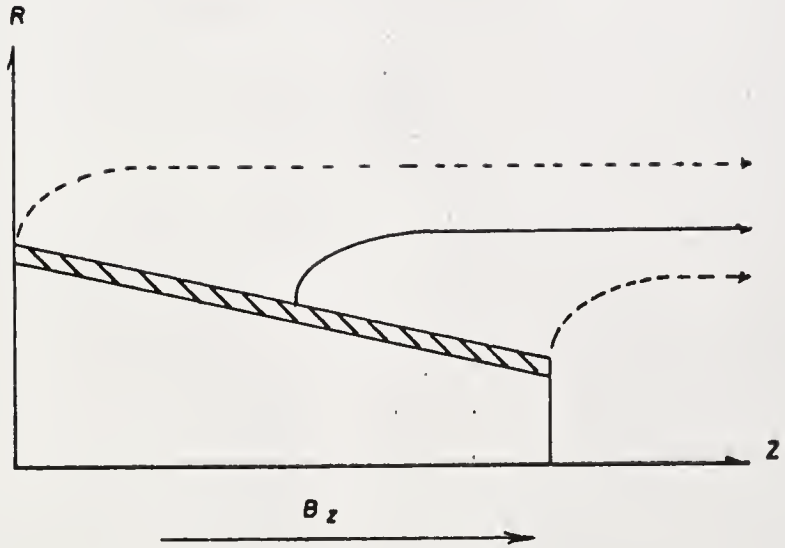


Figure 5. Typical Electron Trajectories for a Truncated Magnetron-injection Gun

plane, first located at the cathode apex and continuously moved along the $+z$ axis.

The forces acting on the beam in the gun region in the absence of a grid are:

1. An outward force due to the radial component of electric field.
2. An axial force due to the axial component of electric field.
3. A θ directed force due to interacting of the radial velocity component with the axial magnetic field.
4. An outward centrifugal force due to rotation about the axis.
5. An inward force due to the interaction of the θ velocity component with the axial magnetic field.
6. Outward force due to space-charge.

After the beam is injected into the drift tube, the electric field force is due only to space-charge. Using Gauss' theorem, the field at the edge of the beam due to space-charge can be calculated.

$$\epsilon \oint_S \vec{E} \cdot \vec{da} = -2\pi\epsilon r \frac{d\phi}{dr} = Q \quad \begin{array}{l} \text{(Charge inclosed in} \\ \text{the beam per per} \\ \text{unit length)} \end{array} \quad (3)$$

And for a total beam current I and voltage V_0 , the radial field is given by

$$\frac{d\phi}{dr} = \frac{-I(r)}{2\pi\epsilon r \sqrt{2\eta V}} \quad (4)$$

where

r = radial coordinate in the beam

$$Q = \frac{-I}{\dot{z}_e}$$

\dot{z}_e = axial electron velocity = $2\eta V$

$$\eta = \frac{|e|\hbar}{m} \quad \text{have been used.}$$

From (4) above, it is noted that the electric field and force on the outer electron shell is greater than the force on the inner shell; therefore, for a balanced flow condition, the outer shell must rotate such that $\dot{\theta}$ (outer shell) $>$ $\dot{\theta}$ (inner shell). This difference in angular velocity will produce a shear in the beam; consequently, the conclusion is drawn that any grid system so located as to partition the beam azimuthally could cause beam break-up in the drift region. A single cathode strip arrangement and its projection on the $r - \theta$ plane is shown in Figure 6.

Suppose now that a non-emitting ring is located concentric with and in the center of the cathode as illustrated in Figure 7a (such a non-emitting ring would be created by a negative grid ring located above the cathode surface). A projection of this ring onto the $r - \theta$ plane produces a pair of concentric hollow beams

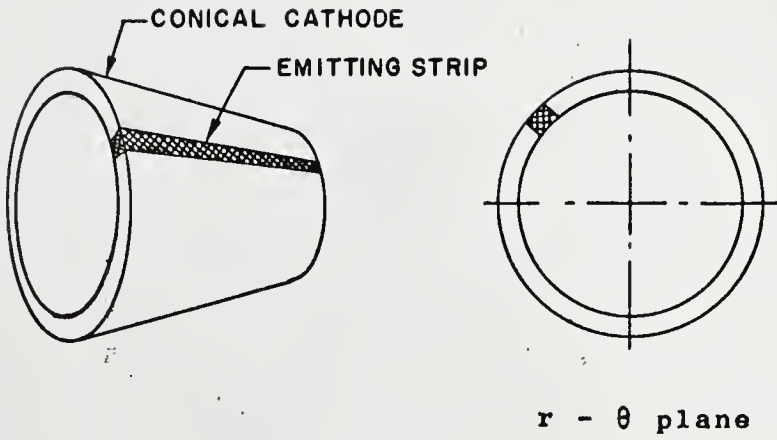


Figure 6. Projection of an Emitting Strip onto the $r - \theta$ Plane

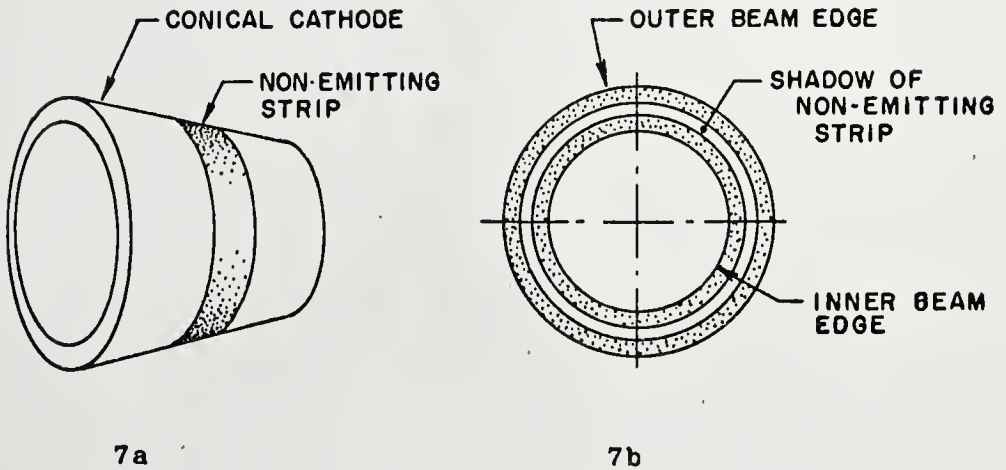


Figure 7. Projection of Non-emitting Strip from a Conical Cathode onto the $r - \theta$ Plane

as illustrated in Figure 7b. This projection pattern appears to have the proper symmetry for a well-defined beam in that shear produced by slight angular velocity differences does not distort the pattern. However, to build and support a grid system which so shadows the cathode in only an axially periodic manner presents a complex engineering task. The problem is one of mechanically supporting each grid ring while electrically operating all rings at the same potential yet electrically isolated from the cathode. Any interconnecting wire would partition the beam in an azimuthal direction in the projected view. Grid construction and experimental evaluation of two systems similar to the above are discussed in Chapter III and Appendix B.

Cathode Mask Ratio

A very important triode parameter to consider before analyzing any one specific grid configuration is the grid-to-cathode mask ratio.¹ Consider the case of an electron emitted from a conical cathode magnetron-injection gun immersed in an infinitely strong, axially

¹The definition used in this dissertation for grid-to-cathode mask ratio is the ratio of the ray projection of the grid area to the cathode area in the $r - \theta$ plane.

symmetric, magnetic field, B_z . Movement is restricted to a direction parallel to B_z at the radius of origin since $\dot{\theta}$ of Equation (2) is reduced to zero. To an observer looking at the cathode from a distant point along the positive z-axis, the truncated cathode cone area would appear as a ring with an area of approximately $1/\sin \theta_0$ times the cone area as illustrated in Figure 8. The addition of a grid consisting of concentric rings, located as illustrated in Figure 9, would completely mask the cathode when the grid wire diameter projections overlap on the $r - \theta$ plane. This arrangement would be quite sensitive to magnetic field variations in a practical device and does not seem feasible from the viewpoint of a projected grid mask ratio.

Next, consider the conical grid wire configuration of Figure 10a. For the same set of conditions as above, the grid mask ratio is the ratio of the cross-section area of one grid wire times the total number of wires divided by the cathode area. Its projection onto the $r - \theta$ plane is illustrated in Figure 10b. This arrangement appears feasible from a grid mask ratio point of view since the projected mask ratio is the same as the

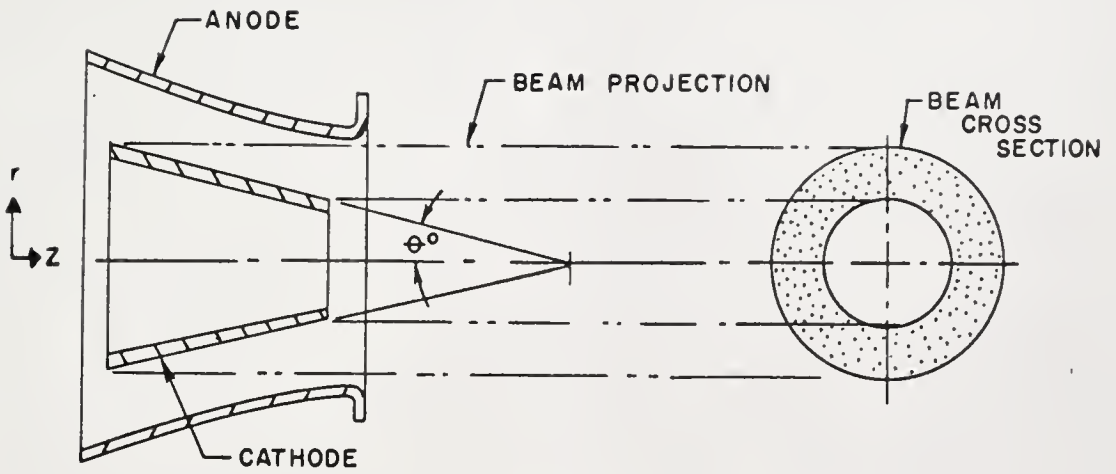


Figure 8. Beam Projection onto $r - \theta$ Plane for an Infinitely Strong Axial Magnetic Field

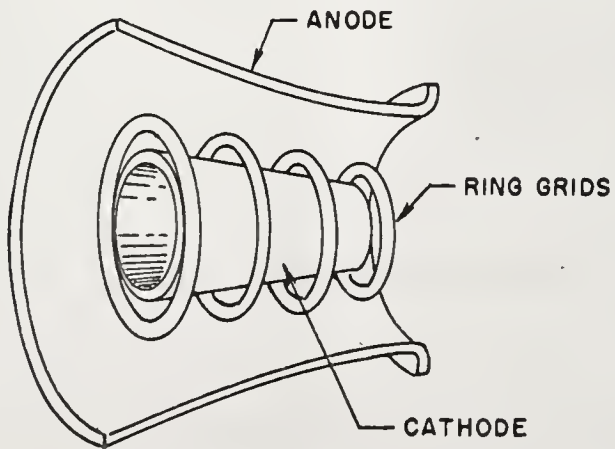
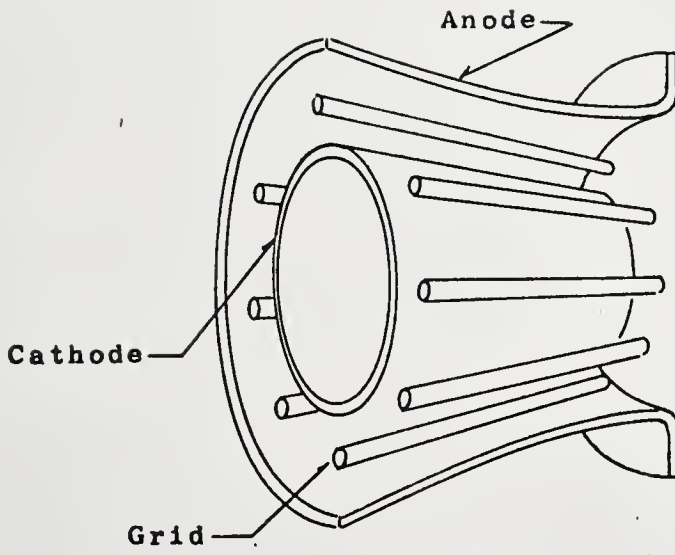
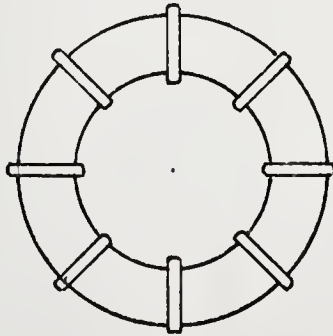


Figure 9. Concentric Ring Grid Structure



10a



10b

Figure 10. Conical Parallel Wire Grid and Projection

screening fraction.¹

Closely associated with grid mask ratio are two other important gun parameters: the gun perveance and cut-off μ .² Although the exact cut-off μ is not a function of magnetic field, the ability to design a "sharp cut-off" triode in the strict sense is possible only to the degree that the current density of emission at the cathode is not a function of magnetic field.

Grid Cut-off μ

The effectiveness of a grid in controlling cathode current is a function of several parameters. These include the height of the grid above the cathode, grid pitch and shape. When electron perturbations are not a design factor, the range of grid μ is from zero to infinity. However, trajectory perturbations in the crossed-field gun impose severe limitations on the grid design from the standpoint of the magnetic field requirements if anode interception is to be prevented. As

¹ Screening fraction is the ratio of the grid cross-sectional area to the cathode area.

² The cut-off μ of a triode is by definition the magnitude of the ratio of anode voltage to grid voltage required to reduce the cathode current to zero.

stated earlier, a normal electron path involves both radial expansion and angular acceleration about the axis of symmetry. A typical electron trajectory is illustrated in Figure 11. Since a negative grid is a non-intercepting grid, the electron must rise above the grid to escape. If this is to occur, the grid cannot be placed excessively above the cathode. Thus, the magnetic field imposes limitations on the cut-off μ .

Consider now a parallel plane approximation for both the concentric grid ring and conical grid structures shown in Figures 9 and 10. Both structures can be represented by the same model; however, the orientation of magnetic field with respect to the grid is different. Examining Laplace's equation in cylindrical coordinates

$$\nabla^2 \varphi = \frac{1}{r} \frac{\partial}{\partial r} \left(r \frac{\partial \varphi}{\partial r} \right) + \frac{1}{r^2} \frac{\partial^2 \varphi}{\partial \theta^2} + \frac{\partial^2 \varphi}{\partial z^2} \quad (5)$$

we see that if r is large compared to Δr in the region of interest, then the Laplacian becomes

$$\nabla^2 \varphi = \frac{\partial^2 \varphi}{\partial y^2} + \frac{\partial^2 \varphi}{\partial z^2} \quad (6)$$

where y has replaced r for the planar approximation. Using this approximation and replacing the round grid wire with rectangular vanes, the model assumes the

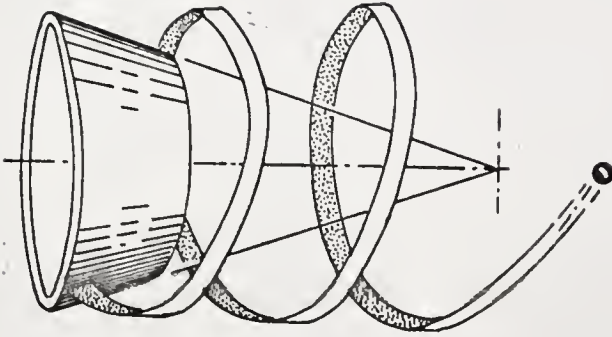
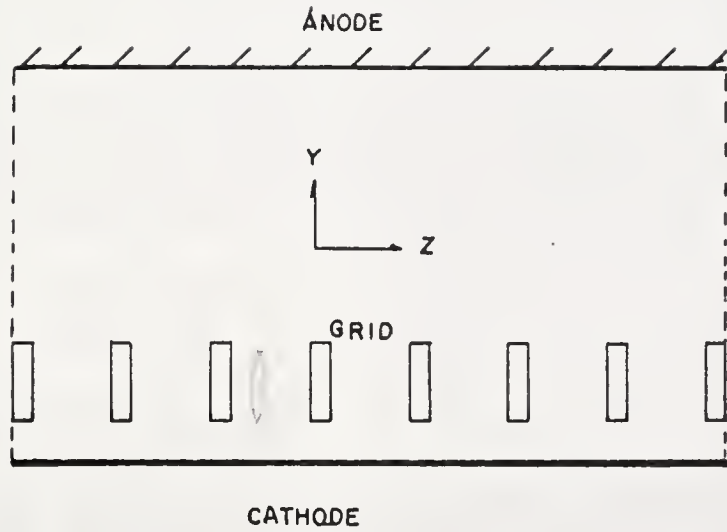


Figure 11. Typical Electron Movement About the Cathode of a Crossed-field Gun

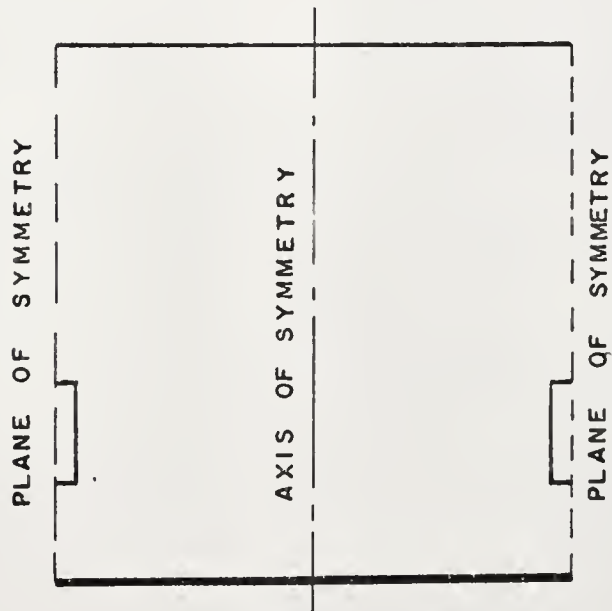
geometry given in Figure 12a. Substitution of rectangular vanes is required for both structural reasons and the desire to minimize lens aberrations by suppression of cathode emission beneath the grid. The model has several planes of symmetry. A single symmetry cell is illustrated in Figure 12b. Since the cut-off μ is independent of magnetic field, it can be determined by solving Laplace's equation for the particular value of negative grid voltage which just reduces the off-cathode potential gradient along the symmetry axis depicted in that figure.

For a sharp cut-off grid transfer characteristics, each cell or segment of a cell must cut-off simultaneously. Examining the electrical contours established in Appendix A for the prototype diode magnetron-injection gun, it is observed that the cathode anode separation is not uniform along the cathode. The separation decreases as the exit end of the cathode is approached; therefore, the grid height and/or pitch must be altered to keep the cut-off constant. The magnitude of this effect became apparent during experimental evaluation.¹ This evaluation showed that as the grid was biased to cut-off

¹The measurement techniques are presented in Chapter III.



(a)



(b)

Figure 12. a) Planar Model of Parallel Vane Grid

b) Single Cell of Symmetry

electron emission from the front (small end) of the cathode decreased more rapidly than from the center and rear sections. A constant μ design based on a tapered grid vane is discussed in Appendix B.

Perveance Reduction Factor

To the author's knowledge, no analytical expression has been published for the determination of cathode current density distribution for the model of Figure 12, even in the absence of magnetic field. Erickson and Sutherland [13] have published a digital computer analysis of non-laminar space-charge flow which establishes self-consistent solutions of Poisson's equation, the equation of electron motion, and the equation of current continuity when the conditions on the boundary are fully specified. It was through an improved version of their program¹ that the form of the current density distribution along the cathode in the absence of magnetic field was established.

Computer Program. - The computer program is formulated to handle the problem of analysis rather than

¹The program actually used is a program presently being developed by Dr. A. D. Sutherland for the Sperry Electronic Tube Division, Gainesville, Florida.

synthesis. A synthesis program would, in general, deal with problems of generating suitable boundary shapes and potentials to produce a given flow pattern. Analysis seeks self-consistent solutions of Poisson's equation of current continuity, when the conditions on the boundary are fully specified.

The boundary conditions for the planar model of Figure 12 are simple. A complete solution involves only the region between a plane of symmetry and an axis of symmetry.

The values of current density and current density distribution along the cathode surface are first estimated. The peak current can never be greater than that for the prototype diode. The computer starts with this assumed current density distribution and then solves Laplace's equation for $\varphi(r,z)$, subject to the specified boundary potentials. Knowing φ and the electron entrance conditions, the equations of motion are solved for the position coordinates of each electron. Space-charge density is then computed based on these position coordinates and the whole procedure is repeated, using Poisson's equation, until a convergence criterion is satisfied.

Formulation of Initial Cathode Current Density

Distribution. - The cathode current density specification can be approximately determined by solving Laplace's equation for both the prototype diode and triode. This solution is obtained through analogue techniques such as an electrolytic tank. Equipotential plots of each model are compared at a particular equipotential on the triode plot where the variation in potential from the plane of symmetry to the axis of symmetry is about 5%.¹ This particular equipotential is then designated as a false anode. The ratio of triode to diode false anode potential raised to the three-halves power permits the calculation of a cathode current density correction term. For example, Figure 13 shows an electrolytic tank plot of the cylindrical negative grid model examined in this study. The solid lines are the diode equipotentials, and the dotted lines show the distortion of these lines produced by the grid. Based on the 5% criteria, the false anode is located between the 20% and 25% contours. From Child's law, the current density reduction factor becomes

¹The choice of 5% is based on computer results.

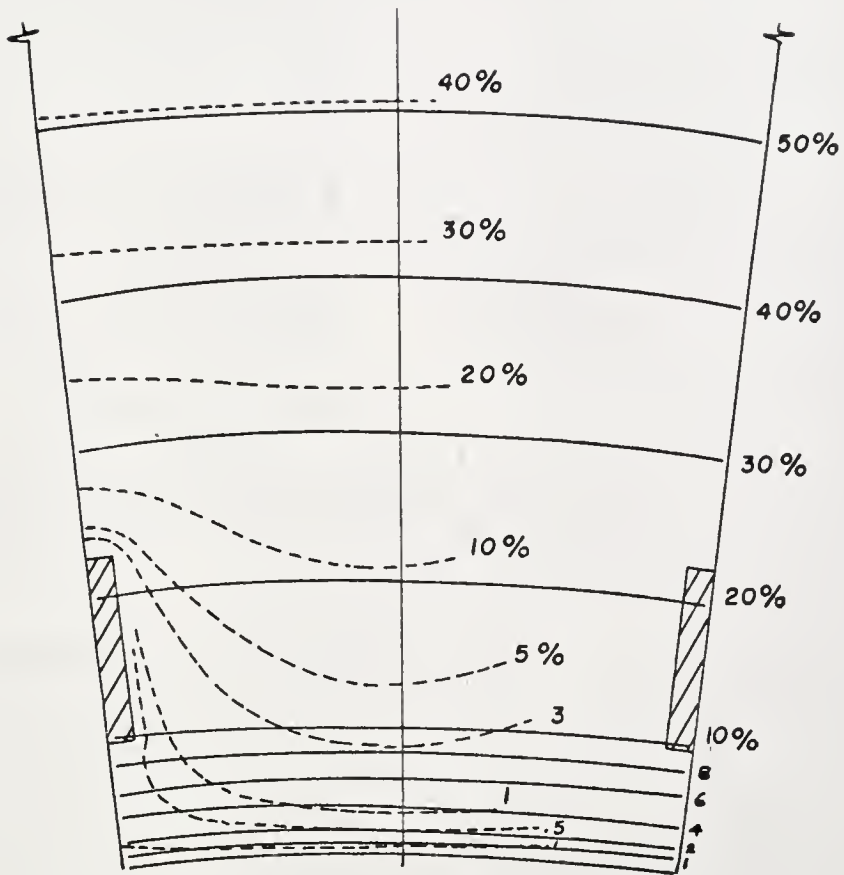


Figure 13. Equipotential Contour Comparison of Cylindrical Diode and Triode

$$\frac{J_t}{J_d} = \left(\frac{\varphi_t}{\varphi_d} \right)^{3/2} \quad (7)$$

where φ_t and φ_d are the % potential values at the false anode location of the triode and diode respectively. This establishes the peak triode current at the axis of symmetry. A current density distribution is then assumed for estimating the current density at all points along the cathode. Since the grid pitch is uniform, the assumed current density distribution function must be a periodic function in z which goes to zero at each plane of symmetry. Based on these criteria, a $\cos^2\theta$ distribution was selected.

Computer Results. - Data presented in this section were calculated for the case of zero magnetic field in the gun region. The deviation of the actual computed cathode current density distribution from the assumed $\cos^2\theta$ function is shown in Figure 14. Curve 4 is based on the diode peak current. Curve 3 is a corrected estimation for this problem based on a 40% equipotential. Curve 2 is the computed curve and curve 1 is the $\cos^2\theta$ approximation. Electron numbers along the abscissa indicate test electron positions along the cathode. Figure 15 shows the non-laminar nature of the electron trajectories in the presence of a grid with space-charge

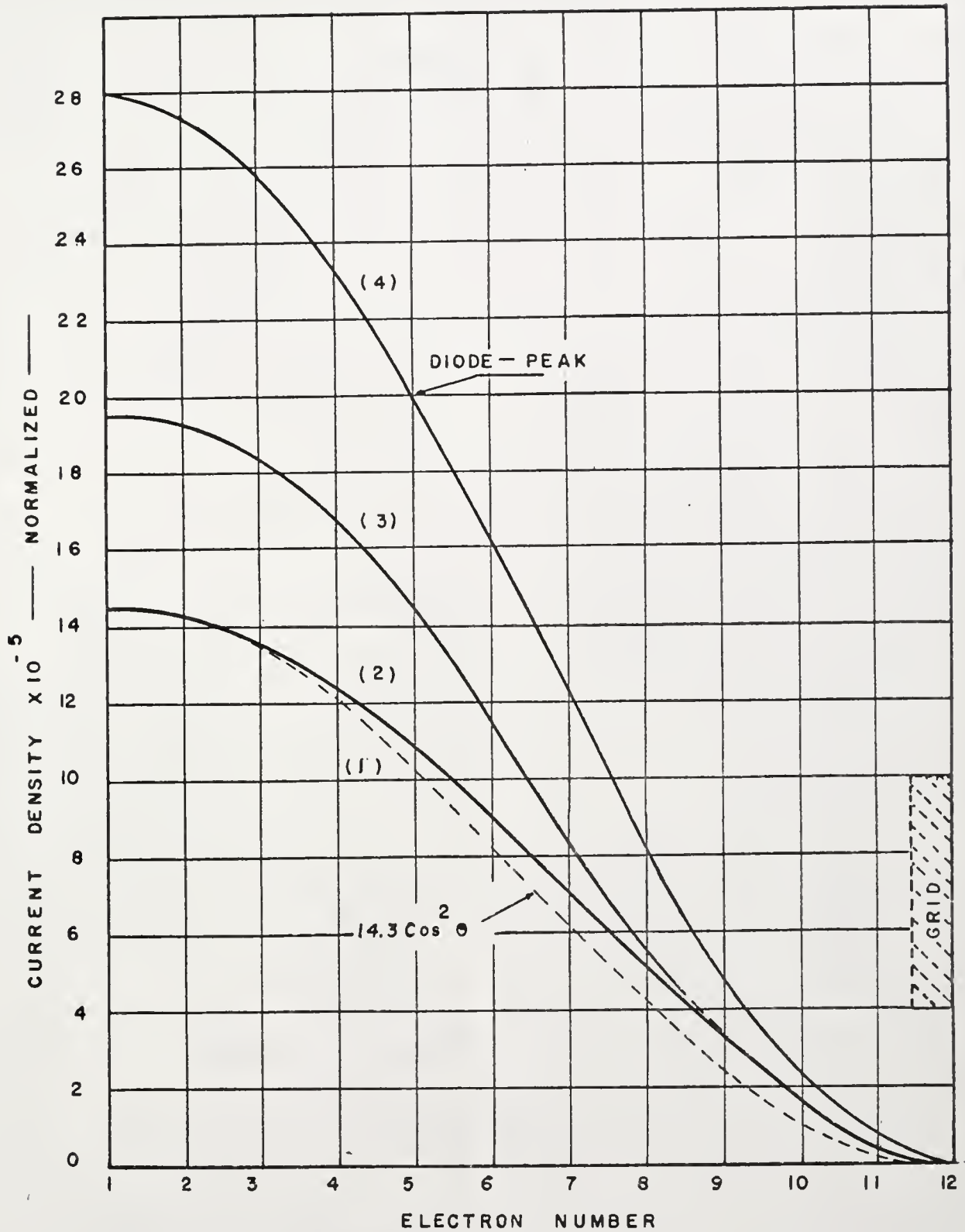


Figure 14. Comparisons of Cathode Current Density Distribution (Ref. Fig. 12)

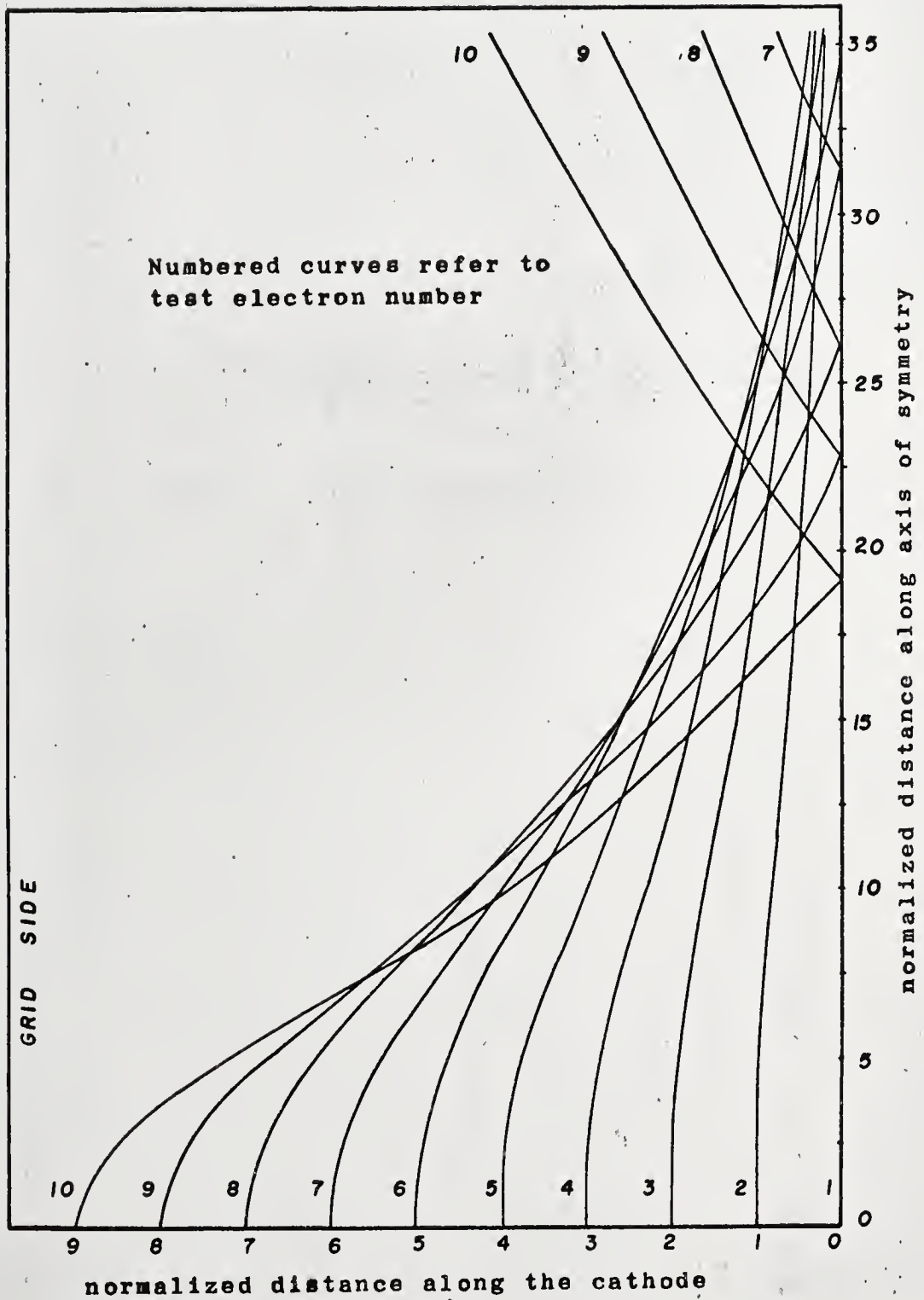


Figure 15. Computed Trajectories with
Space-charge in the absence
of Magnetic Field

effects included. Reflections at the axis of symmetry indicate actual axis cross-over. The true trajectory is simply a reflection of these trajectories at the intercept points along the axis of symmetry.

Analysis of these data immediately showed that the perveance reduction factor computed in the absence of magnetic field was not appropriate for estimating the perveance reduction factor with magnetic field included. Experimental results showed that the grid configuration analyzed had an average perveance reduction factor of approximately 35%. This is contrasted with a peak computed value of 51% at the axis of symmetry. The average reduction is greater than this. This lack of correlation prevented further utilization of the computer program in this analysis because the present program will not treat the case where the cathode and magnetic field intersect at a small angle. However, some very useful information resulted from the data obtained and is discussed below.

The following discussion is a heuristic argument which explains the reason for the difference in measured versus computed perveance reduction data. Referring back to Figure 14, it is noted that even in the presence of space-charge, electrons cross the axis of symmetry. This

means that directly above the section of the cathode least shadowed by the grid is a concentration of space-charge. Associated with this space-charge is a substantial potential depression. Figure 16 is an equipotential plot with space-charge included. Figure 17 is the Laplacian solution. A comparison of the two exemplifies the potential depression produced by the space-charge. However, had a magnetic field been included in the program, the electron trajectories would not have converged nearly as much. Because electrons tend to follow magnetic lines of flux, the Lorentz forces would have caused a more linear trajectory path from anode to cathode. Further, in the actual magnetron injection gun, the electron focal plane may well be outside the gun region since there the electrons are accelerated axially.

The fact that a reduced perveance reduction factor results from the inclusion of magnetic field, suggests that the perveance of the negative grid Pierce-type guns can be increased by permitting flux to thread the cathode along normal trajectory lines.

Note that [2] notes that this effect was not observed in experiments with negative grid Pierce-type guns operating with flux at the cathode.

1 R Ashby 20 Dec 197

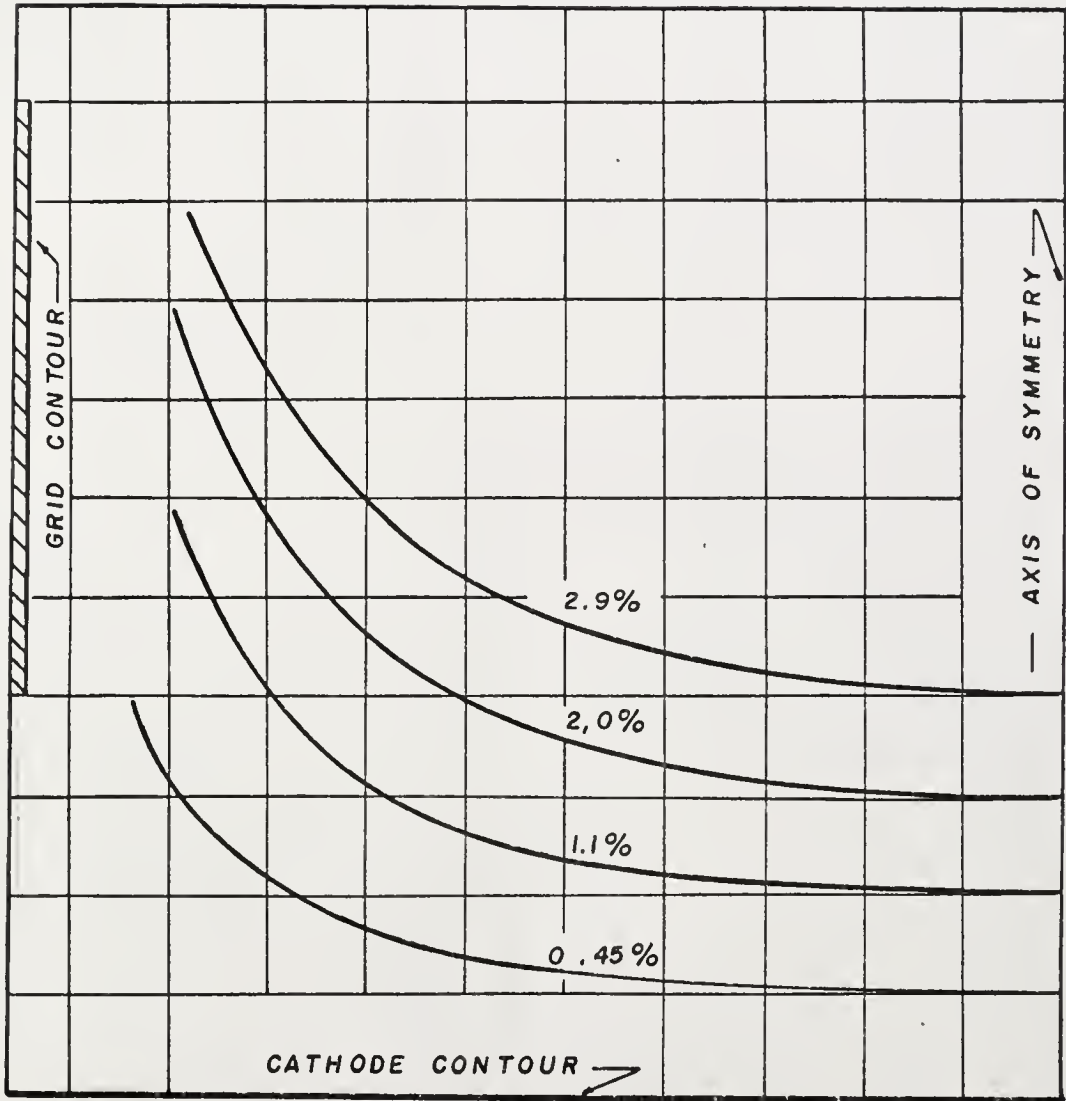


Figure 16. Equipotential Contours with Space-charge (% lines refer to anode voltage)

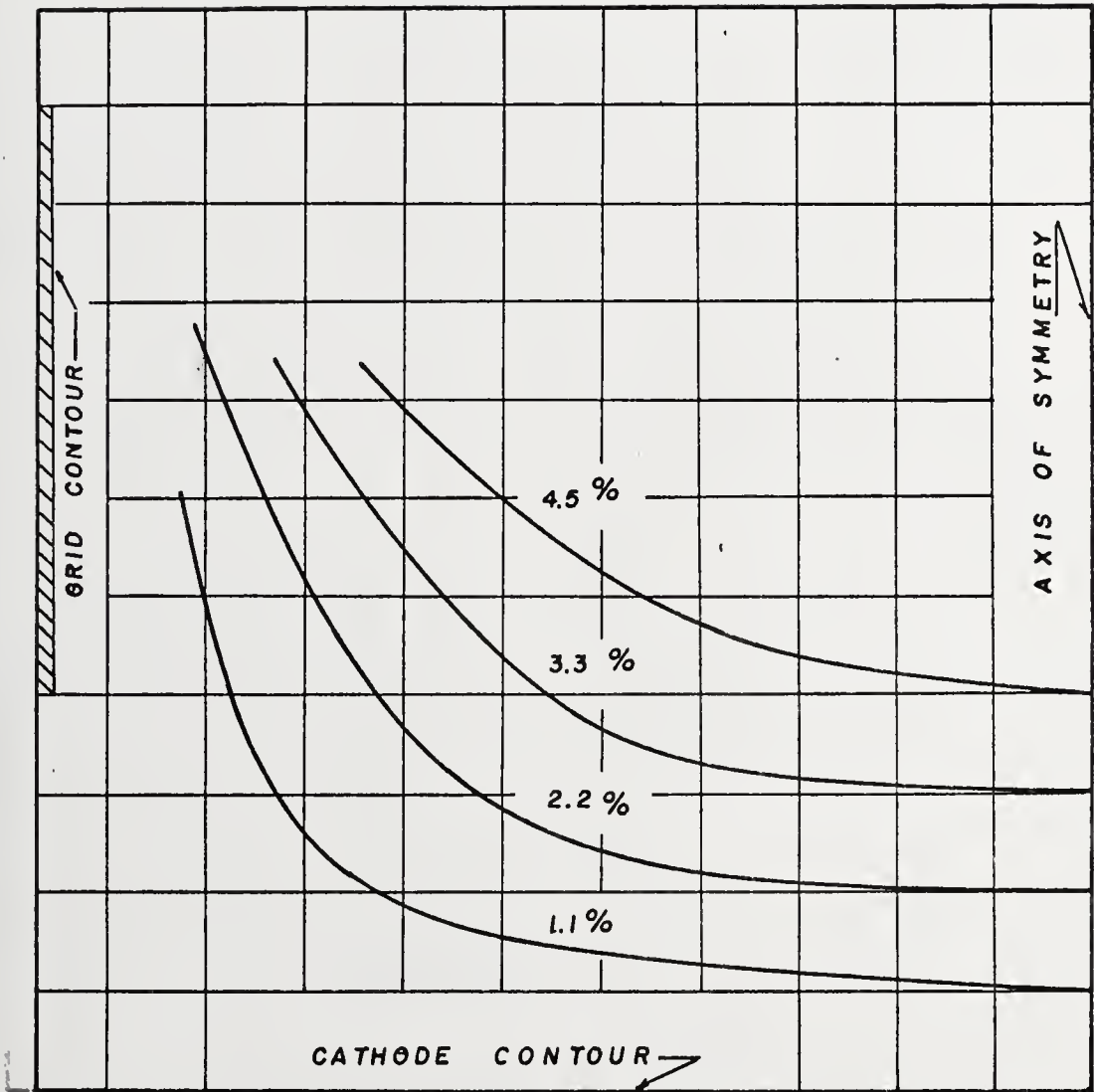


Figure 17. Equipotential Contours without Space-charge
(% lines refer to anode voltage)

Beam Precession

Focusing arguments require that the electrons of an electron beam collimated by a magnetic field all precess about the axis of symmetry or that they rotate about flux lines and have a precessing motion about the axis. Brewer [14] presents a complete discussion of this motion for hollow and solid beams. However, the detection and measurement of this motion has presented quite a challenge. In fact, it has been reported by the Litton Electron Tube Corporation [15] that although calculations indicate beam rotation must be present, it had not been measured. Their conclusions were that perhaps the type of focusing applicable to the magnetron-injection gun was not known! This is a paradox because, when the cathode is completely immersed in the axial magnetic field, one can only conclude that the space-charge forces must cause precession about the axis.

The beam produced experimentally by the radial vane grid is discussed in Chapter III. There it is shown that the beam is broken up into an array of finite diameter line charges. The potential distribution for this situation can be approximated by determining the solution of Laplace's equation for a symmetric array of

line charges of infinitesimal diameter inside of a conducting cylinder. Such an analysis is presented in Appendix B. The resultant potential expression is

$$\varphi(r, \theta) = \frac{-|q_l|}{4\pi\epsilon_0} \ln \left[\frac{\left(\frac{r}{r_1}\right)^{2n} + 1 - 2\left(\frac{r}{r_1}\right)^n \cos n \theta}{\left(\frac{r}{r_0}\right)^{2n} + \left(\frac{r_0}{r_1}\right)^{2n} - 2\left(\frac{r}{r_1}\right)^n \cos n \theta} \right] \quad (8)$$

An examination of Equation (8) reveals that when the radius r corresponds to the radial position r_1 of the line charges, and when the azimuthal position θ also coincides with that of any one of the line charges ($\theta = \frac{2\pi}{n}$), then the potential expression exhibits a pole. These poles exist as a consequence of the approximate representation of a finite diameter line charge with one with infinitesimal diameter. Stated differently, the poles are the consequence of the "self potential" of the line charges themselves. That this is the case can be revealed by an examination of Equation (8) for a region in the immediate vicinity of one of the line charges (say, $\theta = 0$, $r = r_1$).

Let $r = r_1 + \delta$

where δ is a very small number compared to r_1 .

Then, in expression (8), terms involving r can be

approximated to second order through the binomial expansion as

$$\begin{aligned} \left(\frac{r}{r_1}\right)^{2n} &= \left(1 + \frac{\delta}{r_1}\right)^{2n} \\ &\approx 1 + 2n \frac{\delta}{r_1} + \frac{(2n)(2n-1)}{2!} \left(\frac{\delta}{r_1}\right)^2 \end{aligned} \quad (10)$$

$$\left(\frac{r}{r_1}\right)^n = \left(1 + \frac{\delta}{r_1}\right)^n \approx 1 + \frac{n\delta}{r_1} + \frac{n(n-1)}{2!} \left(\frac{\delta}{r_1}\right)^2 \quad (11)$$

The expression for the numerator of the logarithmic term becomes:

$$\text{Numerator} \approx \left(\frac{n\delta}{r_1}\right)^2 \quad (12)$$

Equation (8) can now be written as

$$\varphi(r) \approx \frac{-|q_\ell|}{4\pi\epsilon_0} \ln \frac{\left(\frac{n\delta}{r_1}\right)^2}{\left[\left(\frac{r}{r_0}\right)^n - \left(\frac{r_0}{r}\right)^n\right]} \quad (13)$$

$$\begin{aligned} \varphi(r) &\approx \frac{-|q_\ell|}{2\pi\epsilon_0} \ln(\delta) - \frac{|q_\ell|}{2\pi\epsilon_0} \ln n \\ &\quad + \frac{|q_\ell|}{2\pi\epsilon_0} \ln \left[\left(\frac{r}{r_0}\right)^n - \left(\frac{r_0}{r}\right)^n \right] + \frac{|q_\ell|}{2\pi\epsilon_0} \ln(r_1) \end{aligned} \quad (14)$$

The first term of Equation (14) will be recognized as the potential of the line charge itself, centered at $\delta = 0$, and accounts for the pole. The remaining terms are due to the presence of the other line charges in the array.

Our interest centers upon the motion of any one of

the line charges caused by the presence of all others. This can be evaluated by subtracting from Equation (8) the "self potential" due to the line charge of interest, which is the cause of the pole. Taking the gradient of the resultant expression will yield the electric field due to all other line charges.

Letting $\varphi'(r)$ be the potential resulting from the above operation, we find:

$$\varphi'(r) = \frac{|q\ell|}{2\pi\epsilon_0} \left[-\ln n + \ln \left[\left(\frac{r}{r_0}\right)^n - \left(\frac{r_0}{r}\right)^n \right] \right] \quad (15)$$

$$E'_r = -\nabla\varphi'(r) = \frac{-|q\ell|}{2\pi\epsilon_0} \frac{n}{r} \left[\frac{\left(\frac{r}{r_0}\right)^n + \left(\frac{r_0}{r}\right)^n}{\left(\frac{r}{r_0}\right)^n - \left(\frac{r_0}{r}\right)^n} \right] \quad (16)$$

It should be emphasized that these two equations are valid approximations only when $r \approx r_1$, and $\theta \approx \frac{2\pi}{n}$.

Observe that the radial field along radii which pass through each line charge is negative and finite, resulting in a net outward radial force due to space-charge effects. If the array is restrained by an axially symmetric magnetic field, the line charges will precess about the symmetry axis. In addition to this motion, the electrons in each line charge of finite diameter experience forces associated with the line charge itself.

During the experiments to be described in Chapter III, this particular beamlet pattern, in contrast with a truly hollow beam, permitted observation of beam shear as well as beamlet rotation. Beam precession was detected in accordance with the above theory only after the pulse width of the grid pulse was reduced below 8 microseconds. With a 4.5 microsecond pulse width, beam precession was easily noticeable. It is concluded that ion neutralization, even at vacuums of 5×10^{-8} torr,¹ is sufficient to prevent detection of beam rotation.

¹The beam tester was continuously pumped with an 8 liter ion pump. The indicated vacuum was as stated.

CHAPTER III

EXPERIMENTAL EVALUATION

General

The prototype diode magnetron injection gun was designed from Dryden's [7] theory. A complete design is given in Appendix A. A cross-section of the experimental beam tester used for evaluating the beam formation is shown in Figure 18. Figure 19 shows a photograph of the complete tester unit including solenoid, target drive motor, and mounting rack. Basically, the beam is collimated by the axial magnetic field of the solenoid and impinges on a thin carbonized target located in the telescoping tunnel. The carbonized target used was approximately .003 inches thick and was made by reducing a piece of chemical filter paper in a hydrogen atmosphere. The bellows serve as an axial expansion joint which allows continuous target movement from a plane directly in front of the anode aperture up to 25 centimeters from the anode.

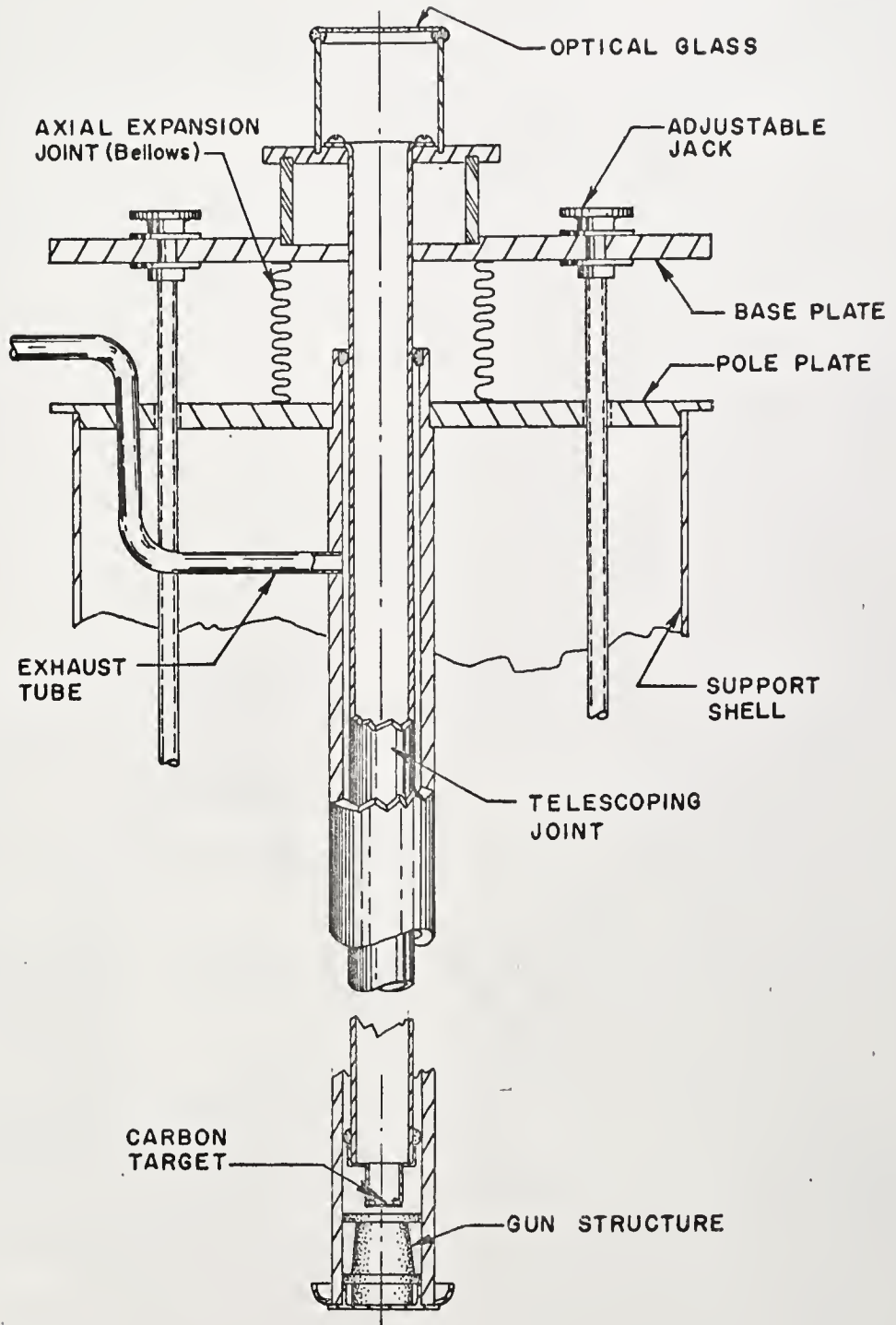


Figure 18. Cross-sectional view of Beam Tester

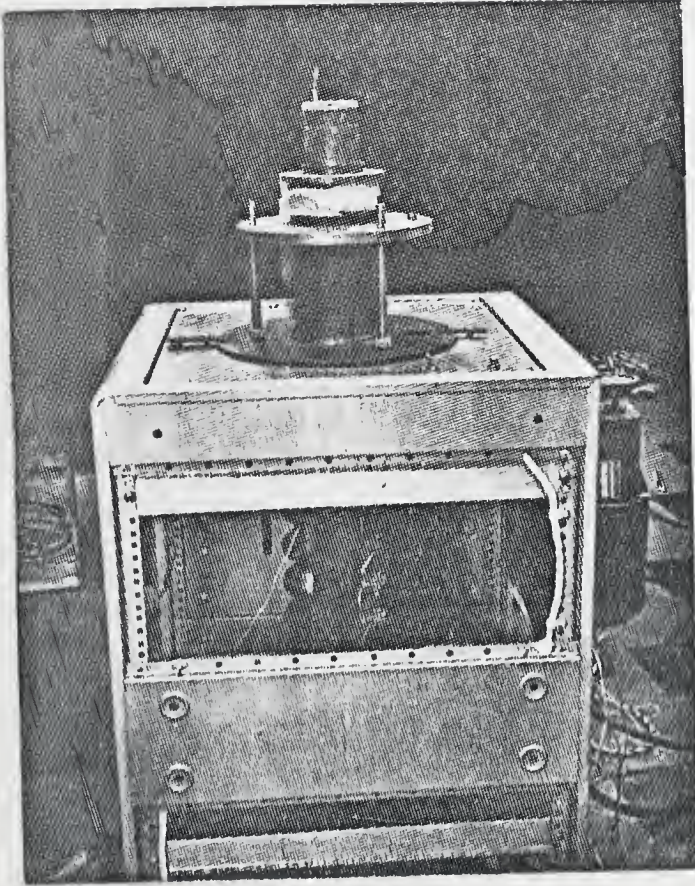


Figure 19. Photograph of Beam Tester

The system is motorized such that the target can be moved very slowly with respect to the gun anode; thereby permitting motion picture photography of the electron impingement (through target luminescence) as well as still photographs to be taken.

The required beam power for observable target luminescence was approximately 5 watts. In order to operate at the design values, summarized in Table 1a, a negative grid modulator was utilized. The grid was pulsed from a condition of grid cut-off up to cathode potential. The target was isolated electrically from all other elements and maintained at a potential positive with respect to the anode potential to prevent secondary electron emission. Measurement accuracy of such an arrangement is somewhat questionable from the standpoint of an exact evaluation of beam size and characteristics. There are two basic sources of error. First, the target imposes an equipotential surface in the tunnel that is not present in an actual microwave device, which alters the electric field in the region of the target. Second, the power required to produce target luminescence is a function of heat transfer by radiation and conduction from the disk target. The rate of decrease in intensity

Table 1a. A Summary of Magnetron-injection
Gun Design Values for the Experimental Prototype Diode

$$\theta_0 = 4^\circ$$

$$J_0 = 204 \text{ ma/sq. cm}$$

$$I = .92 \text{ amperes}$$

$$B = 600 \text{ gauss}$$

$$G = 10$$

$$\phi = .07$$

$$N = 1.275$$

$$V_a = 1220 \text{ volts}$$

$$K_d = 21.5 \times 10^{-6} \text{ amp/volt}^{3/2}$$

of radiation was recently analyzed by Vaidya and Gandhi [16]. Their diagram of relative emission intensity showed that the emission intensity decreases very rapidly outside the beam-illuminated area. However, since a comparison of beam size and shape at various target locations is the primary objective, the errors introduced by the above will cancel and can be neglected.

In each experiment the beam tester was evacuated into a 60 liter/second oil diffusion pump through a liquid nitrogen cold trap. Metal out-gassing was accelerated by baking the tester at an elevated temperature for several hours. An 8 liter ion appendage pump was attached to the tester before bakeout and operated continuously after cathode conversion and removal of the tester from the oil pump. The appendage pump permitted continuous monitoring of pressure as well as pumping.

The axially symmetric uniform magnetic field used in the evaluation of all the experimental guns was established with a long solenoid -- a plot of which is given in Figure 20. The rear of the cathode was located at the point marked K on the graph. On that graph Z_1 and Z_2 depict the range of target movement.

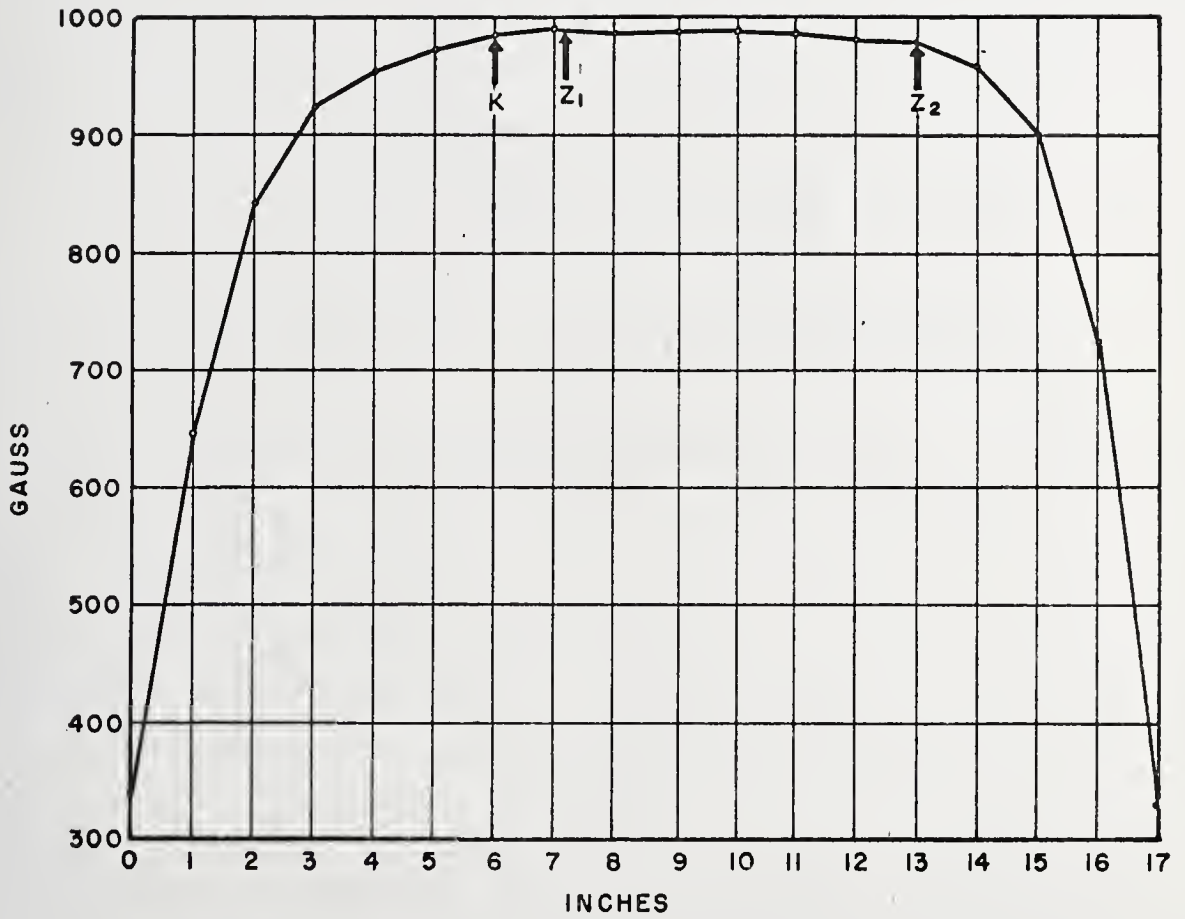


Figure 20. Plot of Magnetic Field used
in Beam Analysis

Experiment #1

The first experiment was to construct and evaluate the prototype diode in the beam analyzer without the grid. A summary of operation is given in Table 1b and Figure 21. A photograph of the beam profile taken at Z_2 , 5.9 inches from the anode exit plane, is shown in Figure 22a. The ratio $\frac{B}{\sqrt{V_a}}$ for this photograph¹ was the design value of 17.1. The slight eccentricity of the beam reflects a misalignment of the cathode to magnetic field axis. The performance of this prototype diode was so close to the predicted values that the misalignment appears negligible. Photographs were also taken at $\frac{B}{\sqrt{V_a}}$ values of 19.8, 23.7 and 27.7, shown in Figure 22b, 22c, and 22d, respectively. It was observed that vorticity and beam breakup resulted from this increase. The instabilities produced are very similar to those observed by Kyhl and Webster [17]. All photographs were taken with a beam power of approximately 5 watts utilizing 20 microsecond cathode pulses.

¹The significance of this ratio is discussed in Appendix A.

Table 1b. A Summary of Prototype Diode Operation

| <u>Anode Voltage (Volts)</u> | <u>Anode Current (ma)</u> | <u>Cathode Current (ma)</u> | $\frac{B}{\sqrt{V_a}}$ | <u>Micro- perveance</u> |
|--------------------------------------|-----------------------------------|-------------------------------------|------------------------|-----------------------------|
| 100 | 2.0 | 26.10 | 13.30 | 26.10 |
| 100 | 1.5 | 24.58 | 14.00 | 24.58 |
| 100 | 0.4 | 24.10 | 14.83 | 24.10 |
| 100 | 0.2 | 21.95 | 16.92 | 21.95 |
| 100 | 0 | 20.83 | 18.83 | 20.83 |
| 100 | 0 | 20.45 | 20.75 | 20.45 |
| 100 | 0 | 20.20 | 22.70 | 20.20 |
| 100 | 0 | 19.90 | 24.78 | 19.90 |
| 100 | 0 | 19.79 | 26.70 | 19.79 |

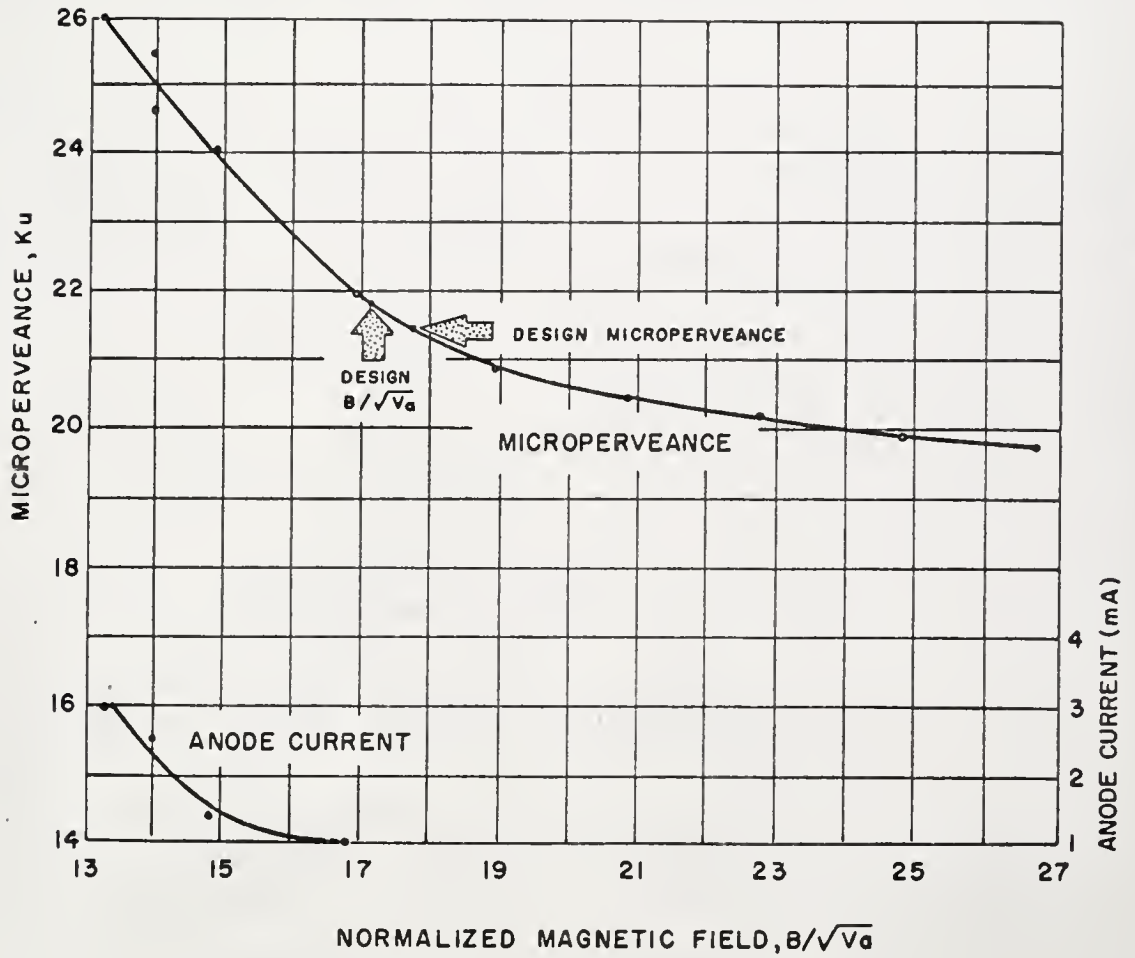
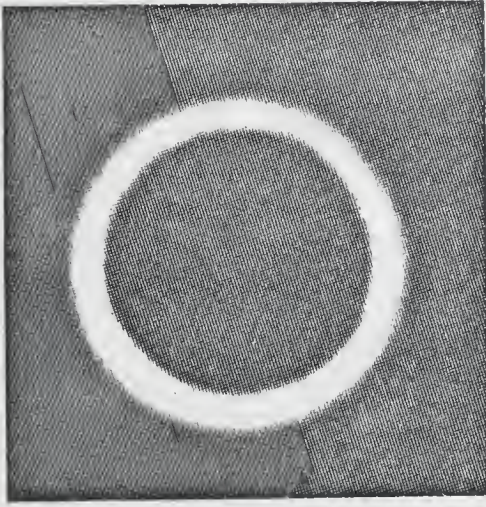
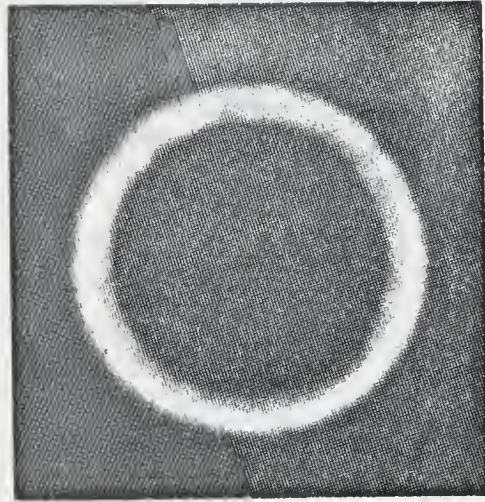


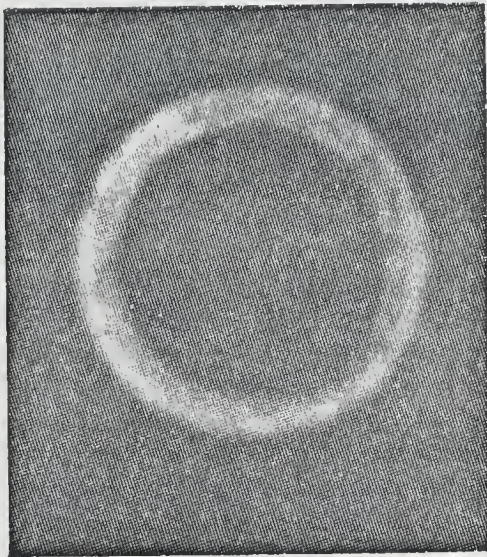
Figure 21. Prototype Diode
Microperveance vs $B/\sqrt{V_a}$ ratio



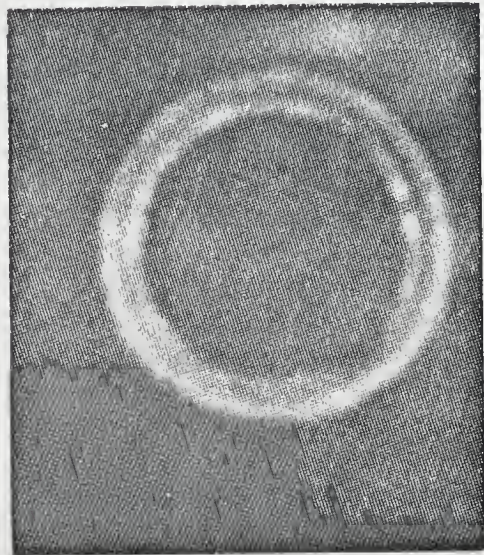
22a



22b



22c



22d

Figure 22. Beam Profile for the Prototype Diode with Magnetic Field Parameter $B/\sqrt{V_a}$ set at a) 17.1 , b) 19.8 , c) 22.7 , d) 27.7

Experiment #2

A photograph of the grid structure used in this experiment is shown in Figure 23a. This structure corresponds to the parallel vane grid model described in Chapter II. The grid vanes are rectangular in cross-section and are supported from the focus electrode. The detailed parts are shown in Figure 23b, where the grid is shown assembled with the cathode. The completed gun assembly, showing support rods and mounting rings, is shown in Figure 24. Details of the grid design procedure are given in Appendix B.

A summary of the experimental data is given in Table 2. These data are also shown plotted in Figure 25. At the design value of $\frac{B}{\sqrt{V_a}} = 17.1 \text{ gauss/volt}^{1/2}$, the anode current is approximately 22 ma corresponding to only 62% beam transmission. The required magnetic field for 100% beam transmission corresponded to a $\frac{B}{\sqrt{V_a}}$ ratio of 22.8 gauss/volt^{1/2}. The perveance at this value was $14.1 \times 10^{-6} \text{ amp/volt}^{3/2}$, which represented a perveance reduction factor of 34.4%. At the diode prototype design value of 17.1, the perveance reduction factor was 8.5%. The required increase in magnetic field for 100% beam transmission represents the degree to which the grid

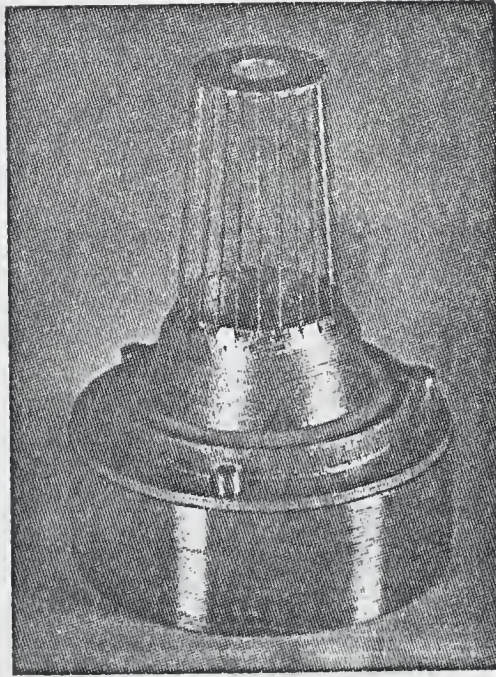


Figure 23a. Vane Grid Structure

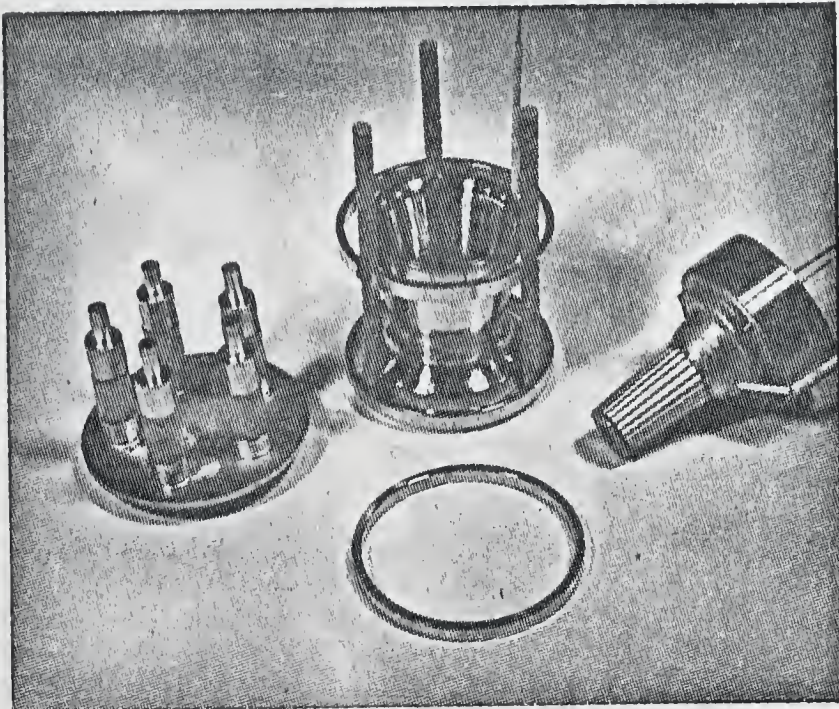


Figure 23b. Component Gun Parts

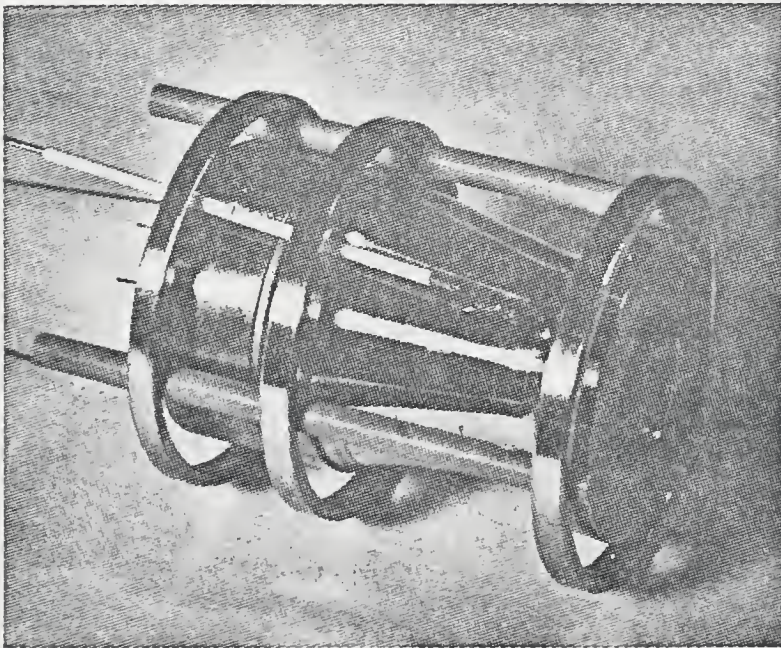
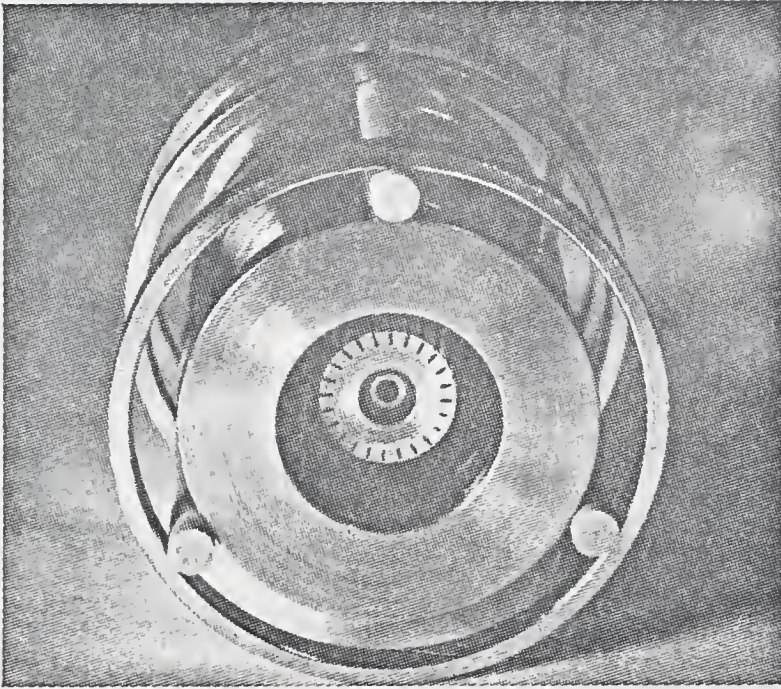


Figure 24. Completely Assembled Vane Grid Gun

Table 2. A Summary of the 24 Vane
Grid Structure Test Data

| <u>Anode Voltage (Volts)</u> | <u>Anode Current (ma)</u> | <u>Cathode Current (ma)</u> | <u>Magnetic Field B (Gauss)</u> | <u>$\frac{B}{\sqrt{V_a}}$</u> | <u>Grid Voltage (Volts)</u> | <u>Micro- per- veance</u> |
|--------------------------------------|-----------------------------------|-------------------------------------|---|--|-------------------------------------|-----------------------------------|
| 200 | 112 | 112 | 0 | 0 | -2 | 42.5 |
| 200 | 109 | 109 | 112.5 | 7.82 | -2 | 38.6 |
| 200 | 99 | 104 | 135.0 | 9.5 | -2 | 36.8 |
| 200 | 91 | 100 | 157.0 | 11.1 | -2 | 35.4 |
| 200 | 40 | 93 | 180 | 12.7 | -2 | 32.9 |
| 200 | 8.0 | 81 | 205 | 14.3 | -2 | 28.7 |
| 200 | 1.3 | 65 | 225 | 15.6 | -2 | 23 |
| 200 | 0.0 | 48 | 270 | 19.1 | -2 | 17 |
| 200 | 0.0 | 40 | 315 | 22.2 | -2 | 14.2 |
| 200 | 0.0 | 38 | 323 | 22.8 | -2 | 13.5 |
| 200 | 0.0 | 37 | 334 | 23.5 | -2 | 13.1 |
| 200 | 0.0 | 32 | 360 | 25.4 | -2 | 11.3 |
| 200 | 0.0 | 28 | 404 | 28.6 | -2 | 9.9 |
| 200 | 0.0 | 26 | 448 | 31.7 | -2 | 9.17 |

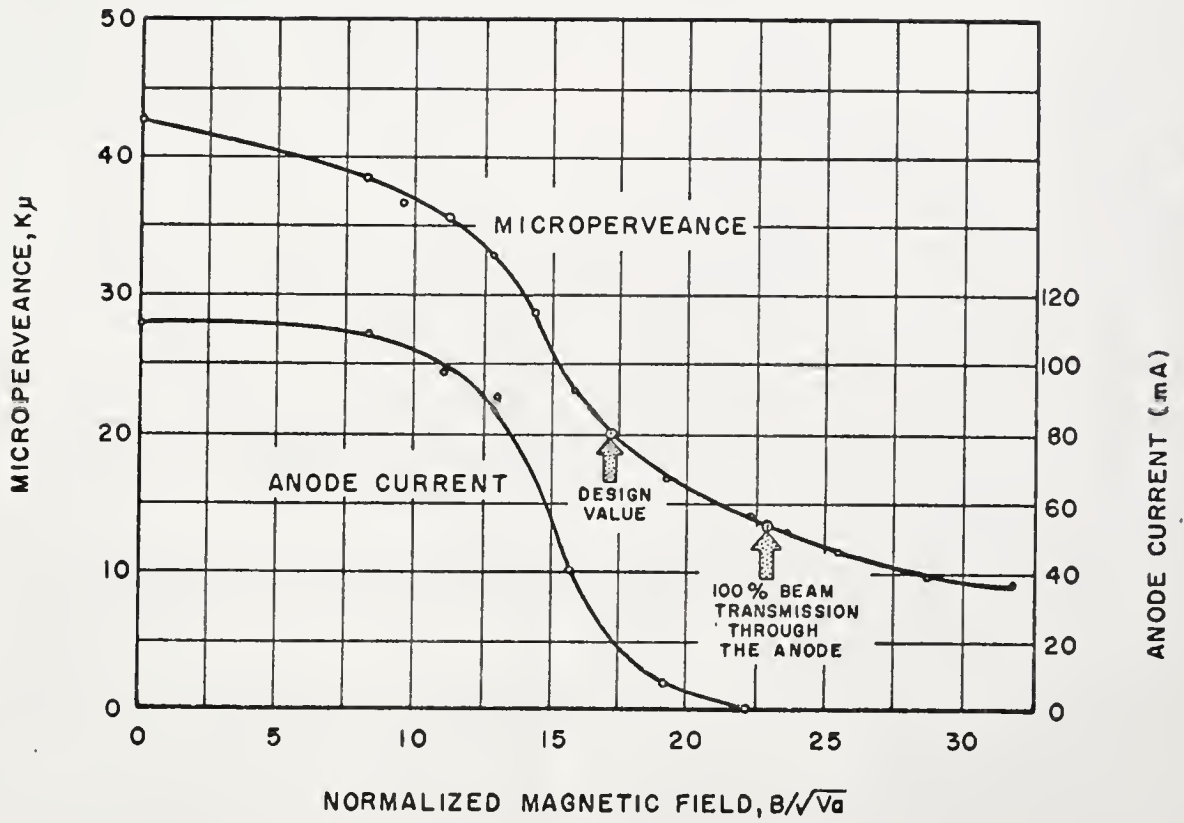


Figure 25. Microperveance and Anode Current versus $B/\sqrt{V_a}$ ratio for the Vane Grid Structure

perturbs the beam in the gun.

Table 3 gives a summary of the grid transfer characteristic data for this structure. These data are shown plotted in Figure 26. The anode voltage was held fixed at the value indicated corresponding to a $\frac{B}{\sqrt{V_a}}$ ratio of 22.8. The $\text{Mu}(95)^1$ average was 9.75.

Photographs of the impingement of the beam on the carbonized target were taken at various distances from the target. A typical beamlet pattern for this structure will be illustrated in later discussion of Experiment #4. These photographs were taken in anticipation of detecting beam precession about the tunnel axis. Later analysis of these photographs showed no net beam precession around this axis; however, it was observed that each beamlet had a characteristic rotation about its own axis. Since this mode of rotation does not provide an inward force to balance the known space-charge forces discussed in Chapter II, an error was apparent or the rotation was too small to detect within the range of the axial target movement. Ion focusing was not suspected at this time as

¹Mu (95) is the ratio of anode voltage to grid voltage required to reduce the current to 95% of its maximum value at $V_g = 0$ volts.

Table 3. A Summary of the 24 Vane Grid
Structure Transfer Character-
istic Data

| Grid Voltage (Volts) | Cathode Current (ma) | | | | | | | |
|-------------------------|----------------------|-----------|-------|-----------|-------|------------|-------|------------|
| | I_k | $V_a=600$ | I_k | $V_a=800$ | I_k | $V_a=1000$ | I_k | $V_a=1200$ |
| $-V_g$ | | | | | | | | |
| 0 | | 180.0 | | 277.0 | | 384.0 | | 560.0 |
| 10 | | 145.0 | | 251.0 | | 350.0 | | 500.0 |
| 20 | | 111.0 | | 211.0 | | 310.0 | | 475.0 |
| 30 | | 79.5 | | 158.0 | | 262.0 | | 395.0 |
| 40 | | 46.2 | | 120.0 | | 212.0 | | 350.0 |
| 50 | | 25.2 | | 79.0 | | 178.0 | | 275.0 |
| 60 | | 9.9 | | 52.9 | | 137.0 | | 237.0 |
| 70 | | 1.6 | | 29.0 | | 92.0 | | 183.0 |
| 80 | | 0 | | 14.5 | | 65.0 | | 120.0 |
| 90 | | | | 6.6 | | 40.0 | | 86.0 |
| 100 | | | | 1.3 | | 22.4 | | 66.0 |
| 110 | | | | 0 | | 13.2 | | 43.5 |
| 120 | | | | | | 6.6 | | 30.0 |
| 130 | | | | | | 2.64 | | 19.0 |
| 140 | | | | | | 0 | | 10.0 |
| 150 | | | | | | | | 2.7 |
| 160 | | | | | | | | 0 |

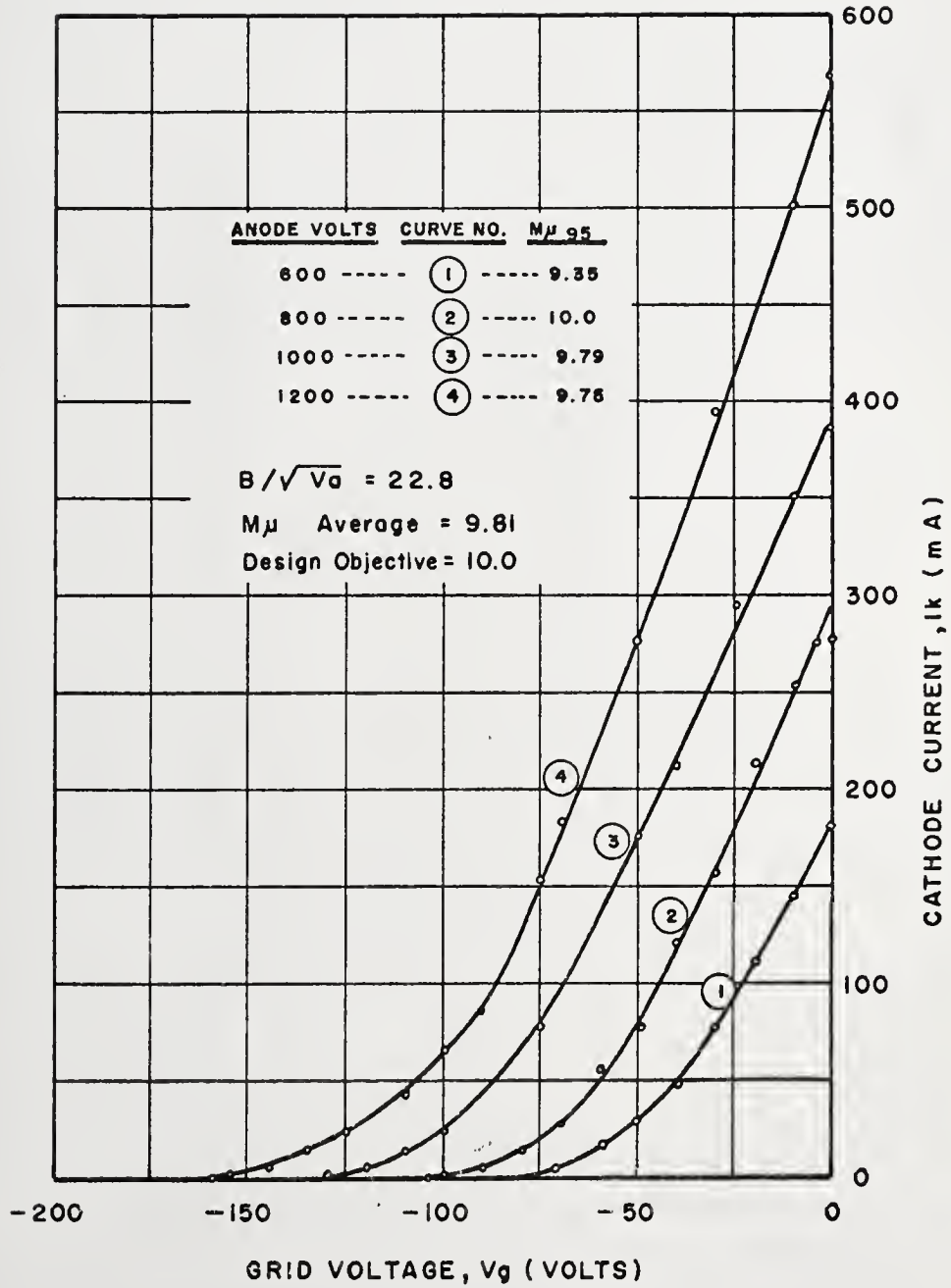


Figure 26. Grid Transfer Characteristics for the Vane Grid Structure

the indicated pressure on the ion gauge of the appendage pump was 8.5×10^{-8} torr. Furthermore, the pulse width of the negative grid pulse had been reduced to approximately 12 microseconds--a pulse duration usually considered too short for ion buildup.

Further beam analysis was accomplished by observing the beam through a telescope with a graduated reticle. The beam size was measured and found to be smaller than the corresponding diode prototype. An average of 10 readings for each diameter is given in Table 4. The smaller size and beam thickness of the measured data is attributed to the stronger magnetic field required to reduce the anode interception to zero in the grided case. The above data were taken at $\frac{B}{\sqrt{V_a}} = 22.8$. Another source of error in beam thickness is probably due to a shadowing effect of the grid support ring into which the 24 grid vanes are terminated. This ring was designed to function as a front focus electrode. However, the exact location of the ring with respect to the cathode front edge was at best an approximation of a normal focus electrode for a truncated cathode and could easily have suppressed electron emission from a small portion of the cathode front edge, thereby producing both a thinner beam and reduced perveance.

Table 4. Calculated Versus Measured Beam Size

| | <u>Calculated</u> | <u>Measured</u> | <u>% Error</u> |
|----------------------------|-------------------|-----------------|----------------|
| Beam - Outside Diameter | 0.495 inch | 0.475 | 10.4 |
| Beam - Inside Diameter | 0.392 inch | 0.382 | 10.2 |
| Beam Thickness | 0.0515 inch | 0.0415 | 12.4 |

Experiment #3

A photograph of the grid structure used in this experiment is shown in Figure 27a. This structure utilized rectangular .004 x .007 inch tape wound helically such that the wide dimensions was facing the cathode. This undesirable orientation was necessitated by mechanical difficulties encountered in attempting to wind the tape in the form of a helix with the narrow dimension facing the cathode.

A summary of the experimental data is given in Table 5. These data are also shown plotted in Figure 28. The degree to which this grid orientation reduced the perveance was surprising. It was somewhat anticipated as discussed in Chapter II, but the amount required experimental verification.

The beam generated by this structure definitely showed breakup. A photograph of the beam breakup only a few centimeters from the anode is shown in Figure 27b. Measurements of beam size were not performed due to the poor beam shape produced.

Table 6 gives a summary of the grid transfer characteristic data for this structure. These data are shown plotted in Figure 29. The anode voltage was held

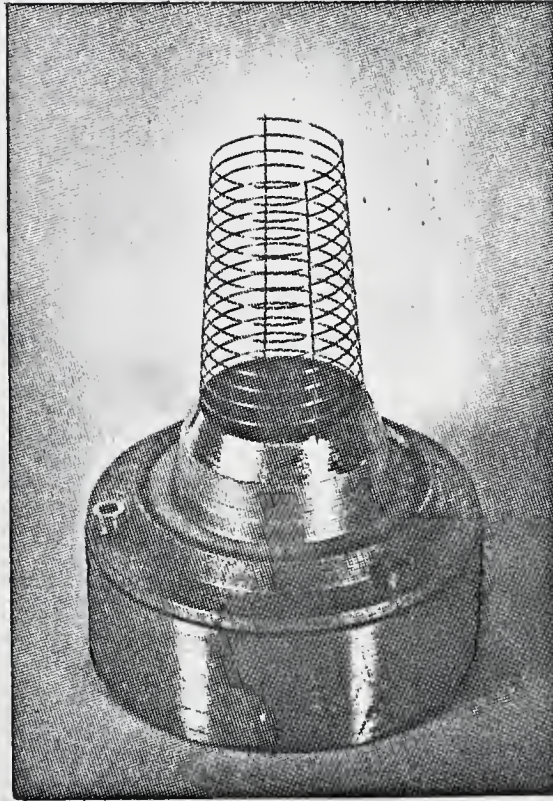


Figure 27a. Photograph of Helical Grid Structure

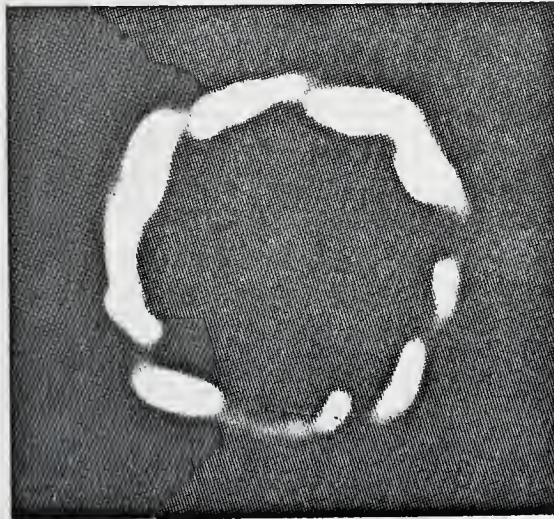


Figure 27b. Photograph of Beam Profile for Helical Grid Structure

Table 5. A Summary of the Helical
Grid Structure Test Data

| <u>Anode Voltage (Volts)</u> | <u>Anode Current (ma)</u> | <u>Cathode Current (ma)</u> | <u>Magnetic Field $\frac{B}{\sqrt{V_a}}$</u> | <u>Grid Voltage (Volts)</u> | <u>Micro- perveance</u> |
|--------------------------------------|-----------------------------------|-------------------------------------|---|-------------------------------------|-----------------------------|
| 200 | 0 | 3.0 | 42.3 | -2 | 1.06 |
| 300 | 0 | 7.5 | 34.6 | -2 | 1.44 |
| 400 | 0 | 17.0 | 30.0 | -2 | 2.13 |
| 500 | 0 | 30.0 | 26.8 | -2 | 2.68 |
| 600 | 0 | 45.0 | 24.4 | -2 | 3.06 |
| 700 | 0 | 67.0 | 22.6 | -2 | 3.62 |
| 800 | 0 | 95.0 | 21.2 | -2 | 4.20 |
| 900 | 0.25 | 130.0 | 20.0 | -2 | 4.80 |
| 1000 | 1.0 | 185.0 | 19.0 | -2 | 5.85 |
| 1100 | 1.3 | 250.0 | 18.1 | -2 | 6.85 |
| 1200 | 2.3 | 330.0 | 17.3 | -2 | 7.94 |
| 1300 | 4.3 | 420.0 | 16.6 | -2 | 8.95 |
| 1400 | 10.0 | 580.0 | 16.0 | -2 | 11.10 |

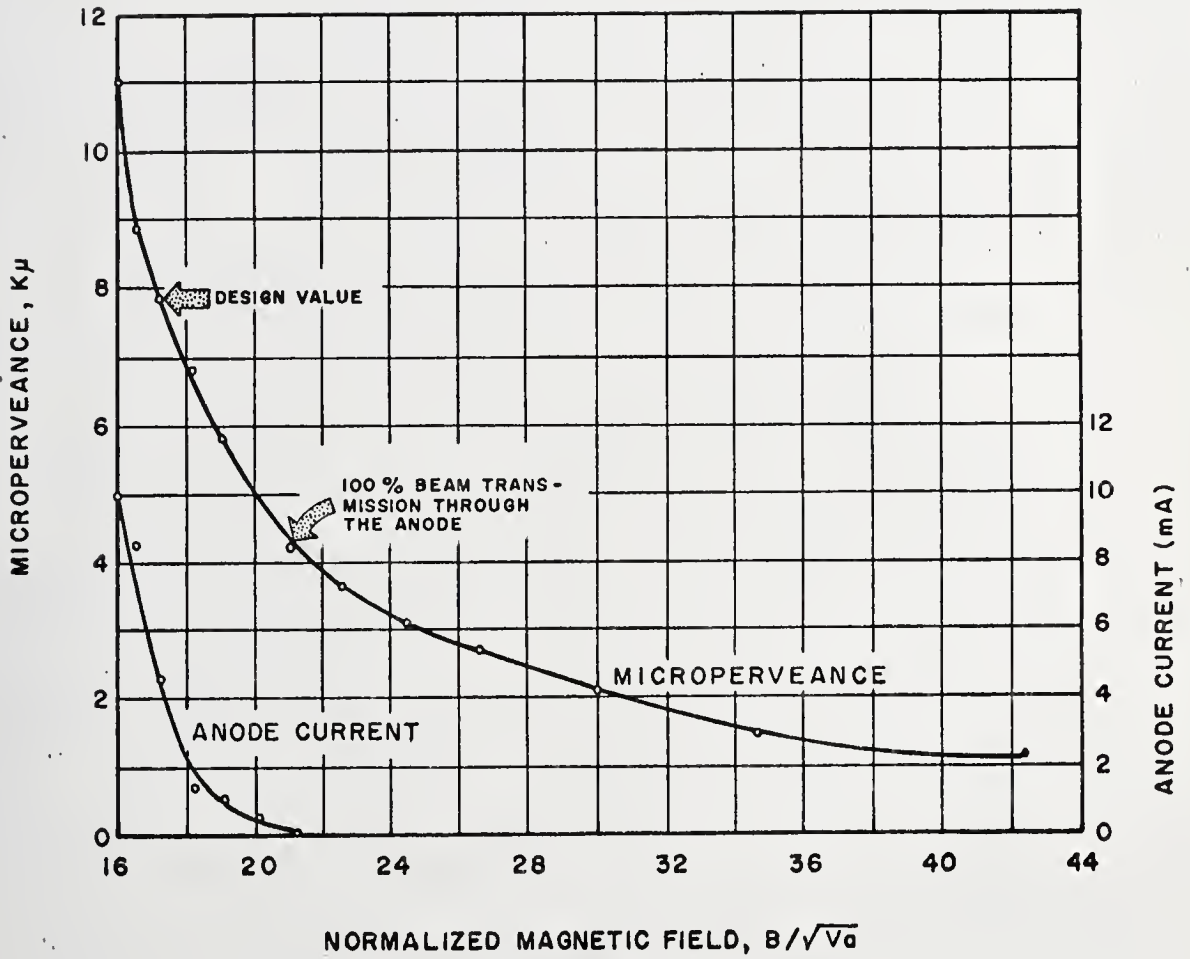


Figure 28. Microperveance and Anode Current versus $B/\sqrt{V_a}$ Ratio for the Helical Grid

Table 6. A Summary of the Helical Grid Structure Transfer Characteristic Data

| Grid Voltage (Volts) $-V_g$ | Cathode Current (ma) | | | | | |
|--------------------------------------|----------------------|-------------|-------|-------------|-------|--------------|
| | I_k | $V_a = 600$ | I_k | $V_a = 800$ | I_k | $V_a = 1000$ |
| 0 | | 101.1 | | 155.0 | | 233.0 |
| 10 | | 81.2 | | 140.0 | | 202.0 |
| 20 | | 62.0 | | 116.0 | | 183.0 |
| 30 | | 50.5 | | 101.0 | | 155.0 |
| 40 | | 38.7 | | 85.0 | | 144.0 |
| 50 | | 32.6 | | 73.5 | | 128.0 |
| 60 | | 21.7 | | 58.0 | | 113.0 |
| 70 | | 15.5 | | 50.4 | | 96.6 |
| 80 | | 10.1 | | 38.7 | | 83.5 |
| 90 | | 3.8 | | 31.0 | | 70.0 |
| 100 | | 1.6 | | 21.7 | | 58.1 |
| 110 | | 0 | | 15.5 | | 46.5 |
| 120 | | | | 10.1 | | 38.7 |
| 130 | | | | 3.86 | | 31.0 |
| 140 | | | | 1.55 | | 20.1 |
| 150 | | | | 0 | | 14.0 |
| 160 | | | | | | 7.75 |
| 170 | | | | | | 4.5 |
| 180 | | | | | | 1.5 |
| 190 | | | | | | 0 |

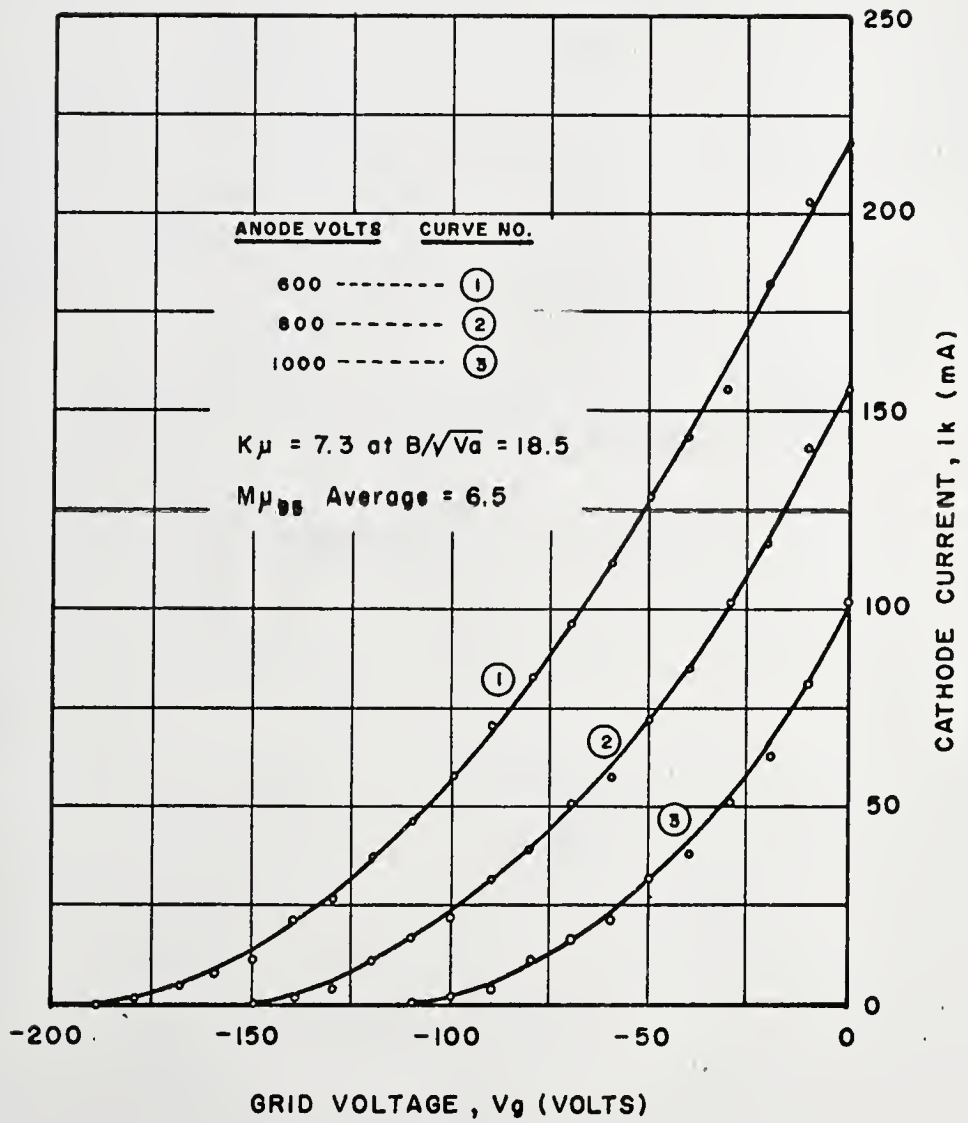


Figure 29. Transfer Characteristics for the Helical Grid

fixed at the values indicated corresponding to a $\frac{B}{\sqrt{V_a}}$ ratio of 18.5 gauss/volt^{3/2}. The Mu (95) average was 6.5.

The perveance reduction factor at the design value of 17.1 amp/volt^{3/2} was approximately 71%. The perveance reduction for zero anode interception was approximately 80%! This gun structure proved clearly impractical.

Experiment #4

This experiment was designed to repeat Experiment #2 with an appropriate grid vane taper for constant cut-off Mu as discussed in Chapter III. A further objective was to re-examine the doubtful data on beam rotation.

The grid modulator was modified to produce pulse widths down to 1 microsecond. The grid structure of Experiment #1 was modified through a potting and grinding operation such that the rectangular grid vanes had a 33% taper. This taper was based on electrolytic tank work representing cross-sections at the small and large ends of the cathode, rather than the average cathode position used in the first experiment. Details of this work are summarized in Appendix B.

The grid transfer characteristics were very

similar to those in Experiment #2 and are not repeated. The anticipated increase in cut-off sharpness and increased perveance reduction factor was partially successful. The perveance attained was $14.7 \text{ amp/volt}^{3/2}$. The grinding and reshaping of the grid structure produced vane pitch variations that prevented the sharp cut-off characteristics expected. The extent to which the vanes are non-uniformly spaced are illustrated in the beam photograph of Figure 30. Although the electron beamlet produced by this structure was irregular in size, the beam profile did not show signs of beam breakup as the target was moved along the axis to a position 5.9 inches in front of the anode. This photograph was made at a beamlet focal point approximately 10 centimeters from the anode.

The beam voltage during measurement was 825 volts. The pulse duration was 4.5 microseconds. The peak target current was 120 milliamperes.

Beam precession was detected at a pulse width under 10 microseconds. Data of beam precession were taken in the form of 35 mm slides every half centimeter for a total distance away from the anode of 16 centimeters. Figure 31b shows a plot of this precession. The rate of

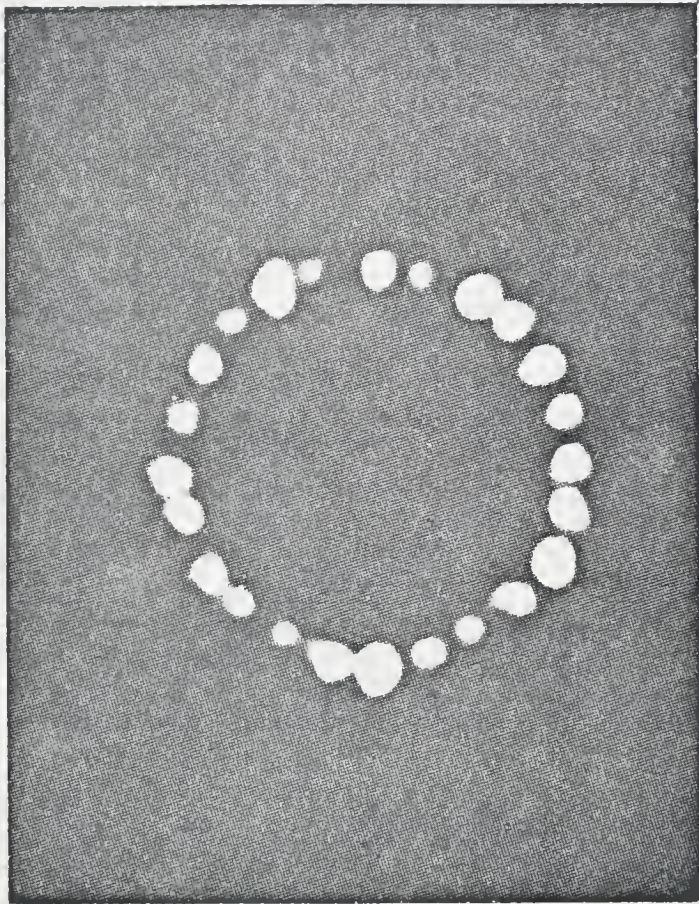


Figure 30. Beamlet Pattern Produced by
the Vane Grid Structure

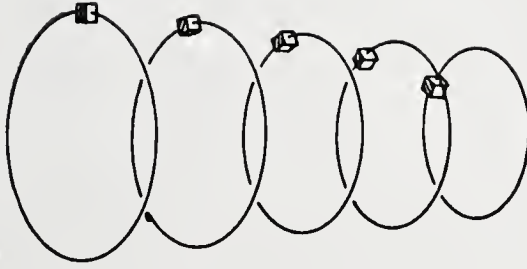


Figure 3la. Typical Precession of a Single Beamlet (Complete Beam Contains 24 Beamlets)

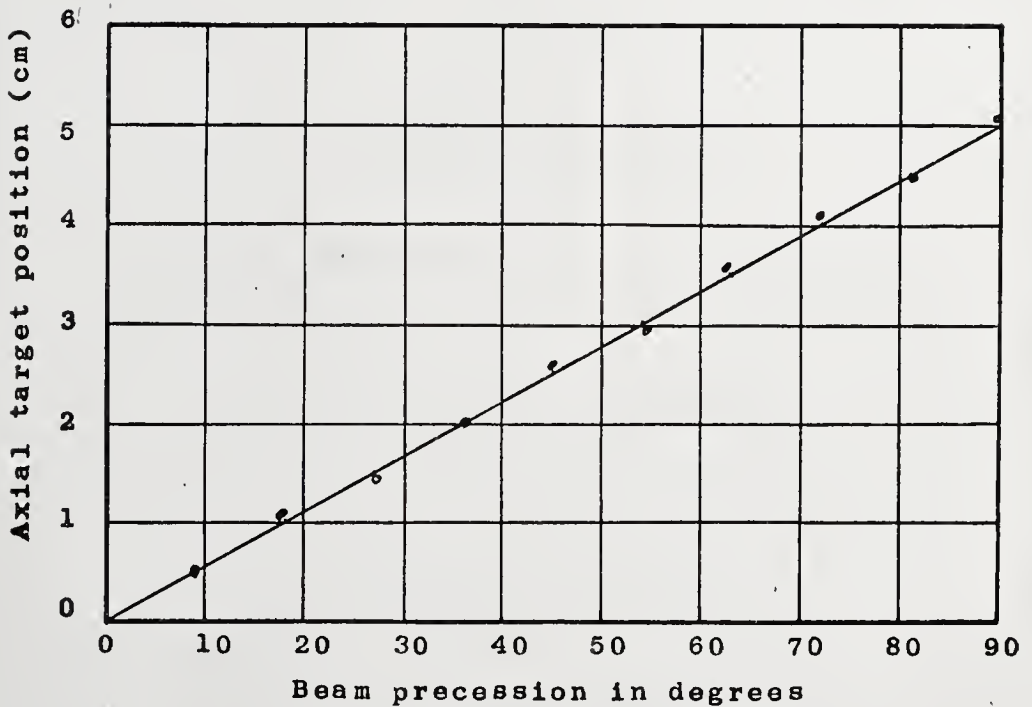


Figure 3lb. Plot of Precession versus Axial Distance (Vane Grid Structure)

precession was approximately $18^{\circ}/\text{cm}$. The manner in which the beamlets moved on the carbon screen is illustrated in Figure 31a. A photograph of the grid current, beam current and grid voltage pulse is shown in Figure 32. The droop in the cathode current at the leading edge of the grid pulse is due to a magnification of the grid pulse by the μ of the structure.

Experiment #5

The purpose of this experiment was to verify that the beam analysis performed and the negative grid design developed can be utilized in an actual microwave amplifier. The traveling wave tube selected was an L-band amplifier with a reputable record of performance.¹ The design change simply entailed the removal of a planar gun and substituting a negative grid magnetron injection gun (radial vane grid type). Pertinent traveling wave tube design parameters are summarized in Table 7. Symbols used in this table conform to those of Pierce [18].

The electronic efficiency for this tube type

¹This tube type is presently in production at the Sperry Electronic Tube Division, Gainesville, Florida.

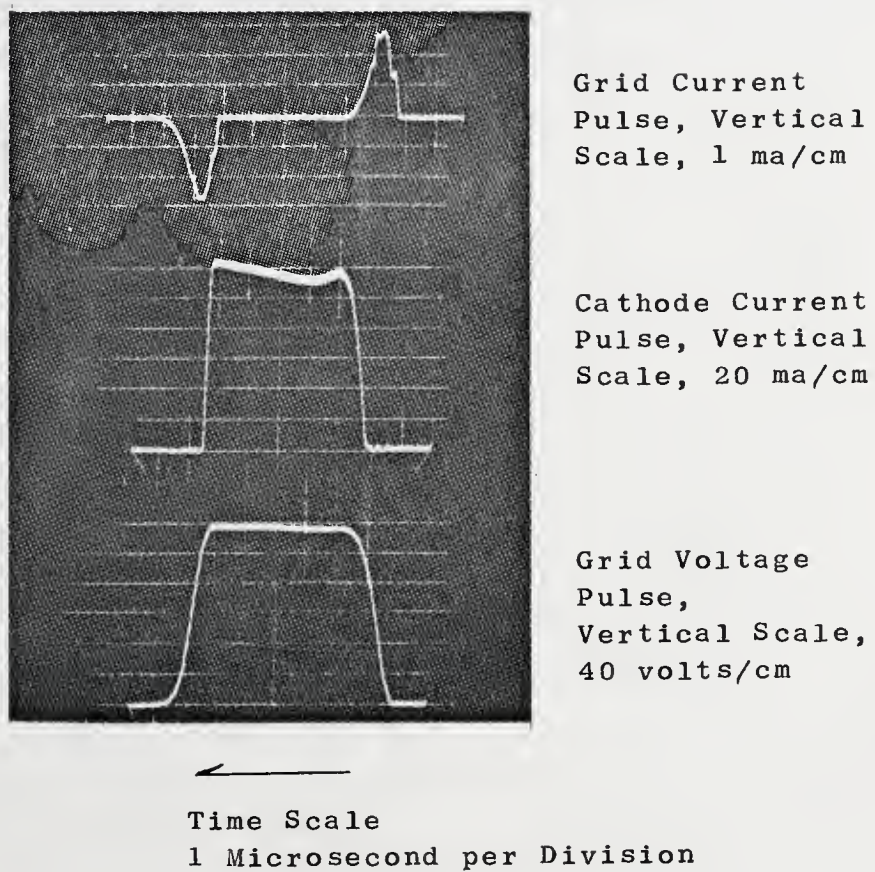


Figure 32. Photograph of Beam Current,
Grid Voltage and Grid Current

Table 7a. Tube Parameters

| Frequency (MHz) | 500 | 750 | 1000 |
|-------------------------------|------|------|------|
| γ_a | 1.55 | 2.32 | 3.1 |
| γ_{r0} | 1.15 | 1.72 | 2.3 |
| Z | 260 | 112 | 54.5 |
| c | .25 | .20 | 1.4 |
| b | 1 | 1.31 | 1.67 |
| 4(QC) | 2.12 | 2.76 | 3.44 |
| B | 41.5 | 39 | 35.5 |
| λ_e (Inches) | 1.77 | 1.18 | .885 |
| Bc/λ_e Gain/Inch (db) | 5.9 | 6.3 | 6.0 |

Table 7b. Typical Beam Parameters

| | <u>Planar Gun</u> | <u>MIG</u> |
|-------------------|-------------------|--------------|
| Beam OD | 0.602 inches | 0.475 inches |
| Beam ID | 0.438 inches | 0.382 inches |
| Beam Current | .862 amperes | 0.5 amperes |
| Beam Voltage | 1900 volts | 2100 volts |
| Efficiency - Peak | 22% | 18% |

utilizing a planar gun is typically 20 - 22% . Rf evaluation of the negative grid design showed a peak efficiency between 17 - 18% . A graph of saturated power output and efficiency versus frequency is given in Figure 33. The beam size of the negative grid magnetron-injection gun was 20% smaller than the original design value for this circuit, which partially accounts (through potential depression) for the reduced efficiency and the increased beam voltage requirement as noted in Table 7b. Additional differences are associated with the higher beam rotational energy in the magnetron-injection gun case.

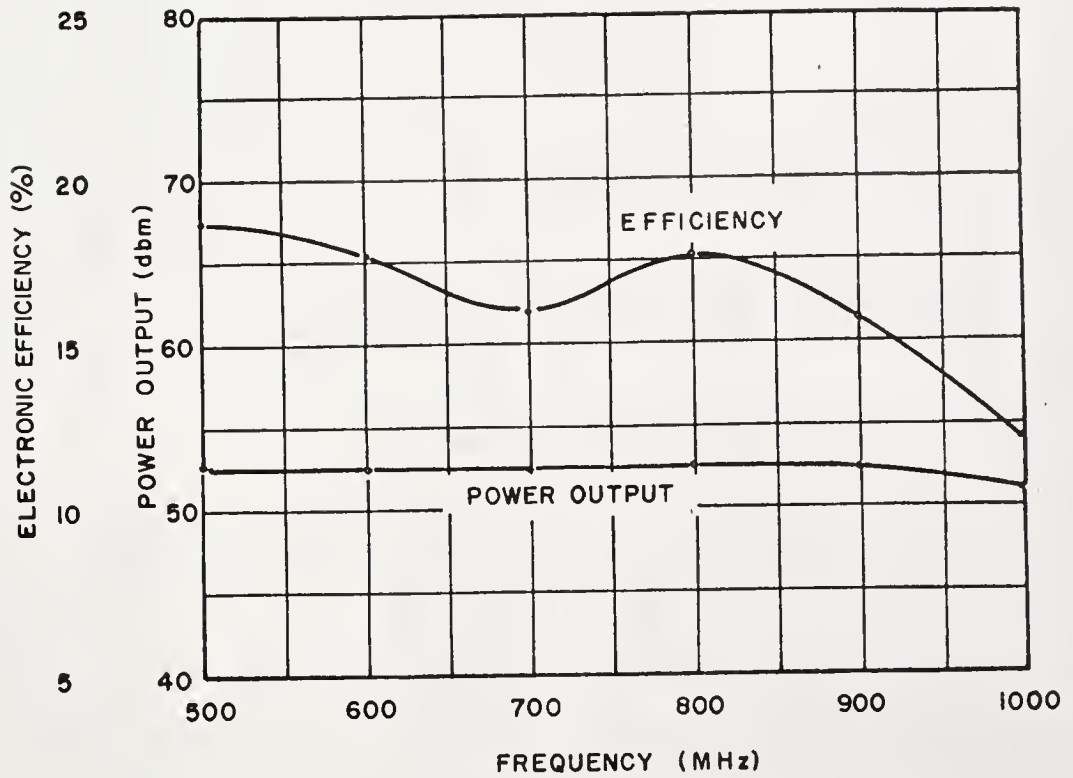


Figure 33. Plot of Efficiency versus Frequency for L-band Tube

(Vane Grid Structure)

CHAPTER IV

CONCLUSIONS

The experimental data reveal that the cathode grid mask ratio, defined and discussed in Chapter II, is the dominant factor influencing the reduction of perveance. In the case of the helical grid, this mask ratio was large, and the perveance reduction was excessive. With the radial vane grid, the cathode mask ratio approached the screening fraction itself (which is clearly the limiting minimum value), and the resultant perveance reduction was considerably less. Another factor entering into the reduction of perveance is the manner in which the presence of the grid perturbs the longitudinal electric field component above the cathode surface. In the case of the helical grid, these perturbations are gross, while with the radial vane grid configuration they are minimized. In the latter case, the longitudinal field component is reduced only in magnitude, but not in direction.

Although the grids evaluated were not perfect from the standpoint of construction and final alignment, experimental evaluation indicates that the negative grid concept can be successfully incorporated in the magnetron-injection gun.

It should be noted that the practical matter of gun alignment in the crossed field gun is a serious and difficult one to accomplish. Variations in the grid plane perpendicular to the cathode are magnified by the area convergence ratio of the gun.

The conclusion with respect to beam precession is that for long pulse or continuous duty operation, the beam is nearly neutralized by positive ions even at an indicated vacuum of 5×10^{-8} torr. This neutralization would suggest that after the beam has been operating long enough for complete ion buildup, the magnetic field could be removed. This is not the case, though, as the electron gun is an excellent ion pump and would be free of ions, thus for proper operation, the magnetic field is still required.

It has been demonstrated that satisfactorily well-defined beams can be obtained from a negative grid crossed field gun. The present understanding of such guns is

largely empirical. Further work is necessary for an exact analysis of beam trajectories in the presence of an axial magnetic field with components both parallel and perpendicular to the cathode.

APPENDICES

APPENDIX A

PROTOTYPE MAGNETRON-INJECTION GUN DIODE DESIGN

The prototype diode design used in the experiments discussed in Chapter III is based on Dryden's theory [7]. As previously stated, Dryden solved the case of an axially symmetric flow from a cone cathode in the presence of an axially symmetric magnetic field. The magnetic field in this analysis is restricted to the uniform field case. Following Kino, Dryden derives the following relationships between the physical quantities and radial variation:

$$\text{Velocity} \quad \mu \approx r^n \quad (\text{A-1})$$

$$\text{Potential} \quad V \approx r^{2n} \quad (\text{A-2})$$

$$\text{Electric Field} \quad E \approx r^{2n-1} \quad (\text{A-3})$$

$$\text{Magnetic Field Intensity} \quad B \approx r^{n-1} \quad (\text{A-4})$$

$$\text{Volume Charge Density} \quad \rho \approx r^{2n-2} \quad (\text{A-5})$$

$$\text{Cathode Surface Current Density} \quad J \approx r^{3n-2} \quad (\text{A-6})$$

where n is an arbitrary constant.

Figure A-1 illustrates a cross-section of a typical truncated magnetron injection gun diode. Truncation means that the cathode does not extend to the cathode cone apex. With the restriction on B (uniform), it is obvious that n in Equation (A-4) must be one. Equation (A-6) is of particular importance since in any design problem the peak cathode current density is a limiting parameter.

Dryden's flow computations were carried out in normalized units of:

$$\text{Time} \quad \tau = t \left(\frac{2\eta J_0}{\epsilon r_0} \right)^{1/3} \quad (\text{A-7})$$

$$\text{Distance} \quad R = \frac{r}{r_0} \quad (\text{A-8})$$

$$\text{Potential} \quad \Phi = V \left(\frac{2\eta \epsilon^2}{J_0^2 r_0^4} \right)^{1/3} \quad (\text{A-9})$$

$$\text{Electric Field} \quad \xi = E_1 \left(\frac{2\eta \epsilon^2}{J_0 r_0} \right)^{1/3} \quad (\text{A-10})$$

$$\text{Velocity} \quad v_1 = u_1 \left(\frac{\epsilon}{2\eta J_0 r_0^2} \right)^{1/3} \quad (\text{A-11})$$

$$\text{Magnetic Field} \quad \omega = \frac{B}{B_0} \quad (\text{A-12})$$

$$G = \eta B_0 \left(\frac{\epsilon r_0}{2\eta J_0} \right)^{1/3} \quad (\text{A-13})$$

where

V is the anode potential

u_1 is the velocity in the 1 direction

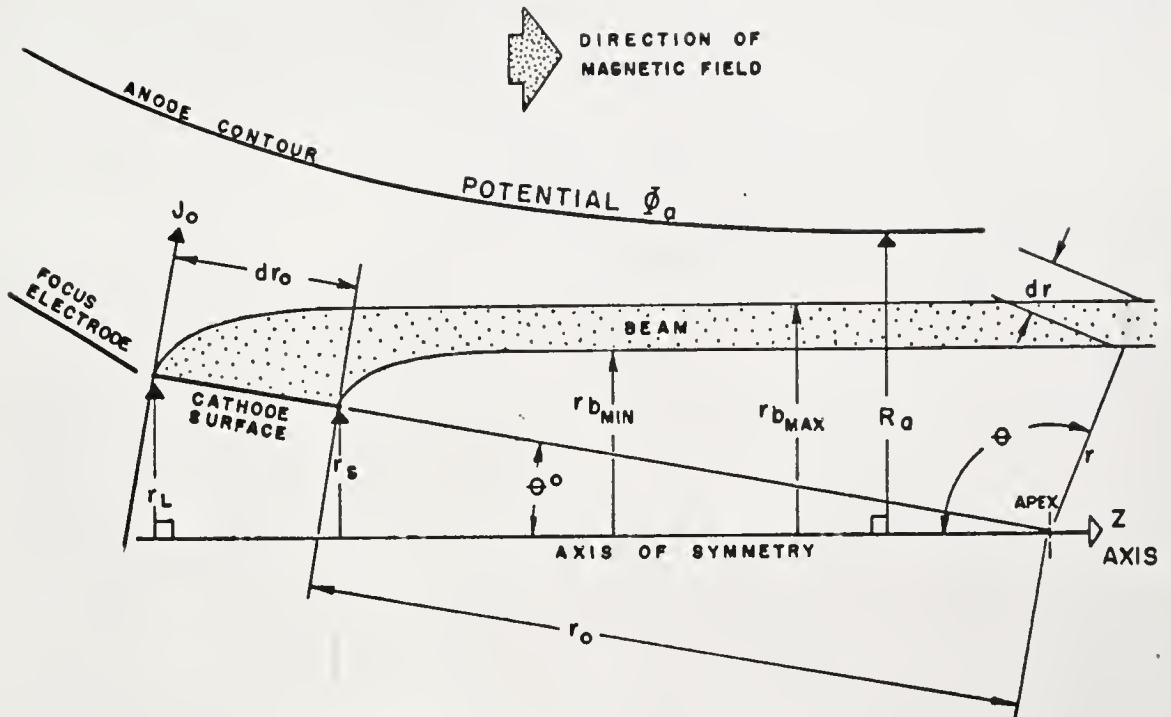
B_0 is the magnetic field intensity at the point (r_0, θ)

G is the magnitude coefficient for the magnetic field

r_0 and other distance symbols are defined in Figure A-1

For the prototype diode, several values of Φ were calculated. These are summarized in Figure A-2, which illustrates the variation of Φ with radius in this theory. The value of Φ determines the diode permeance for a given cathode size and is limited to values greater than the tangential value at the beam edge, since a smaller value which projects into the beam would produce anode interception.

The prototype diode parameters selected for this investigation are given in Figure A-1. The selected cone semiangle, θ_0 , of 4° probably represents a lower limit for the addition of a negative grid. For smaller values of θ_0 , the electron transit time in the gun region becomes excessive, and perturbations of the beam due to lens aberrations caused by the grid would be excessive. An increase in θ_0 would improve grid operation, but reduce area convergence; therefore, 4° seems reasonable to test feasibility. Once a value of Φ and beam thickness have been selected, all other parameters can be specified.



$$N = \frac{r_L}{r_s} = 1.275$$

J_0 = CURRENT DENSITY AT r_0 = 204 mA/cm²

R_a = MINIMUM ANODE RADIUS = .300 in.

r_L = .211 in.

r_s = .166 in.

r_0 = 3.02 in.

θ = 4°

$r_{b \text{ MAX}}$ = .250 in. (CALCULATED FOR $G=10$)

$\frac{R_a}{r_L} = 1.41$ AT CATHODE TEMPERATURE

$d r_0$ = 6.35 in.

$d r$ = .05 in. AT $\theta = 90^\circ$

$r_{b \text{ MIN}}$ = .125 in.

Figure A-1. Cross-section of Truncated Magnetron-injection Gun showing Prototype Diode Design Values

The beam current I emitted from a cone cathode is given in Dryden's theory as:¹

$$I = J_0 \frac{2\pi r_0^2}{3n} (1 - N^{-3n}) \sin \theta_0 \quad (\text{A-14})$$

Solving Equation (A-9) for V permits calculation of the prototype diode perveance. First,

$$V^{3/2} = \frac{\Phi^{3/2} J_0 r_0^2}{2^{1/2} \eta^{1/2} \epsilon} \quad (\text{A-15})$$

Taking the ratio of current, I , to the three-halves power of voltage gives

$$K = \frac{2^{3/2} \pi \eta^{1/2}}{3n \Phi^{3/2}} (1 - N^{-3n}) \sin \theta_0 \quad (\text{A-16})$$

and for $n = 1$

$$K \approx \frac{11 \times 10^{-6}}{\Phi^{3/2}} (1 - N^{-3}) \sin \theta_0 \quad (\text{A-17})$$

The degree of electron expansion after electron emission from the cathode is a function of magnetic field. For balanced flow and a G value of 10, the expansion of each electron follows the path of the shaded area of Figure A-2. The expansion factor for $G = 10$ is 1.16 which produces an average beam diameter 16% greater than the average cathode diameter. Since the perveance will be reduced and the radial beam expansion increased in the

¹ Symbols used are defined in Figures A-1, A-2.

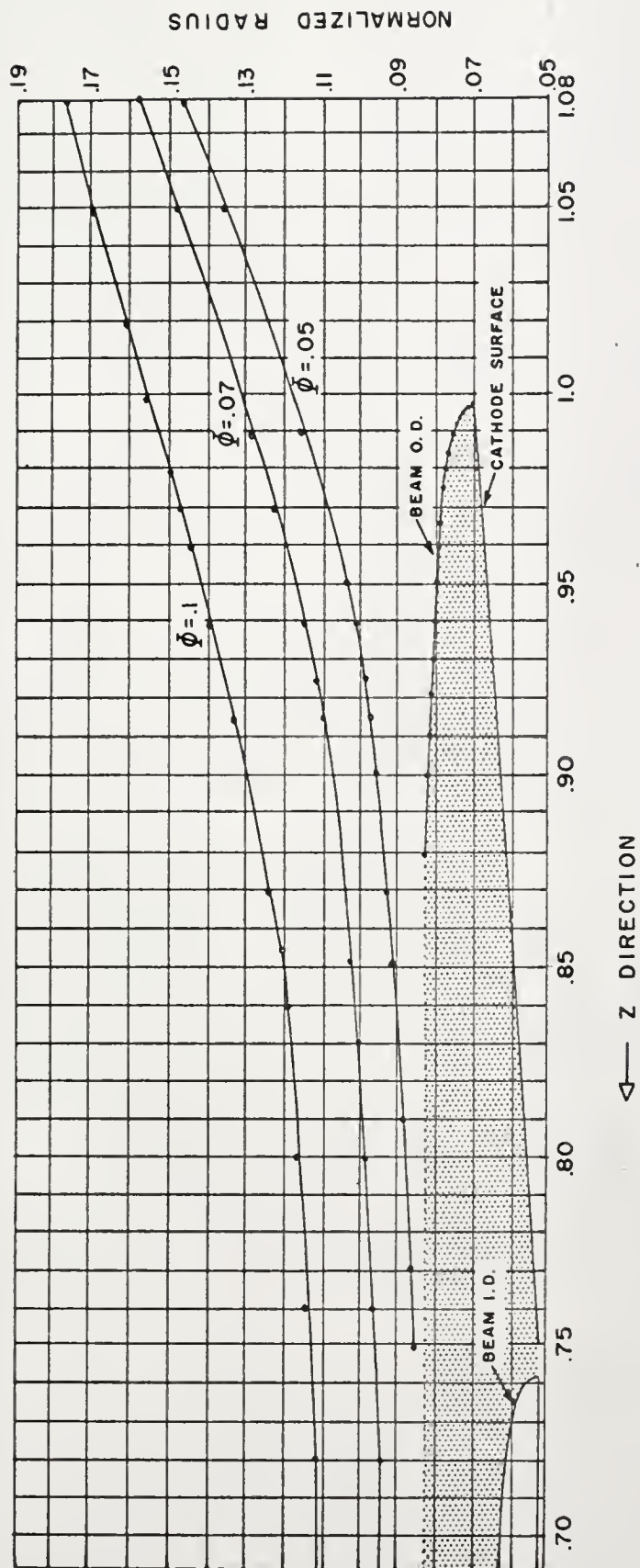


Figure A-2. Normalized Potential ϕ versus z with Electron Emission Profile Shown for Prototype Diode

gun region by the negative grid addition, a value of $\phi = .07$ was selected. Lower values would probably produce anode interception. Substituting $\phi = .07$ and values from Figure A-1 into the perveance expression (A-16) yields a prototype diode microperveance of 21.5. Through the relationship of magnetic field parameter, G , to magnetic field in Equation (A-13), the value of J_0 or B_0 can be calculated depending upon which value is the limiting value in the design. For $B_0 = 600$ gauss and $r_0 = .077$ meters, $J_0 = 204$ ma/sq. cm giving a total current from Equation (A-14) of 0.92 amperes. Knowing the perveance and current, the operating anode voltage can be calculated for the prototype diode since

$$I = KV^{3/2} \quad (A-18)$$

then

$$V = \left(\frac{K}{I}\right)^{2/3} = \left(\frac{21.5 \times 10^{-6}}{0.92}\right)^{2/3} \quad (A-19)$$

and

$$V = 1220 \text{ volts (Anode voltage)}$$

As shown by Dryden, an important parameter in the design of this class of gun is the ratio $\frac{B}{\sqrt{V_a}}$. For the present design, this ratio is

$$\frac{B}{\sqrt{V_a}} = \frac{600}{\sqrt{1220}} = 17.1 \quad (A-20)$$

This completes the prototype diode design. The values selected are typical for hollow beam gun designs used in microwave amplifiers in the 500 to 1500 megacycle frequency band.

APPENDIX B

DESIGN OF EXPERIMENTAL GRID STRUCTURES

Vane Grid Design

The rectangular grid vane was selected as the basic design shape. Structurally, the round wire approach was unsound from the standpoint of grid sag, even with tungsten wire, because of the small diameter of 0.005 inches required for a maximum grid-cathode mask ratio of 10%. Other problems such as suppression of electron emission beneath the grid for a given cut-off μ and minimization of lens aberrations had to be considered.

The design value of cut-off μ was established with an electrolytic tank. A cylindrical, two-dimensional model approximating the conical cathode-grid configuration was established by taking the anode to cathode separation value at the midpoint on the cathode as the cathode-

anode separation of a cylindrical diode. A single grid cell of this concentric cylinder parallel vane structure was then scaled up 100:1 in size and evaluated in an electrolytic tank. Figure B-1 shows a single cell scaled for evaluation. The solid lines illustrate the electrolytic tank equipotential plot of the prototype diode. The cross-hatched area represents the grid location for one cell and the dotted lines show the electric field disturbance as a result of grid operation at cathode potential. It is obvious that little electron emission occurs beneath the grid vanes and that an emission maximum occurs at the midpoint of the cell; also that the % voltage lines are shifted by the grid in a direction to lower the calculated diode current density everywhere on the cathode. Figure B-2 illustrates the cut-off condition for the same structure. The cut-off μ was found to be 8.5.

The grid-to-cathode height was set at 0.010 inches to insure thermal and electrical isolation. The dimensions of the grid were 0.005 x 0.015 inches in cross-section. The separation between grid centers (grid pitch) at midpoint on the cathode was approximately 0.050 inches. Figure B-3 shows a cross-section of the

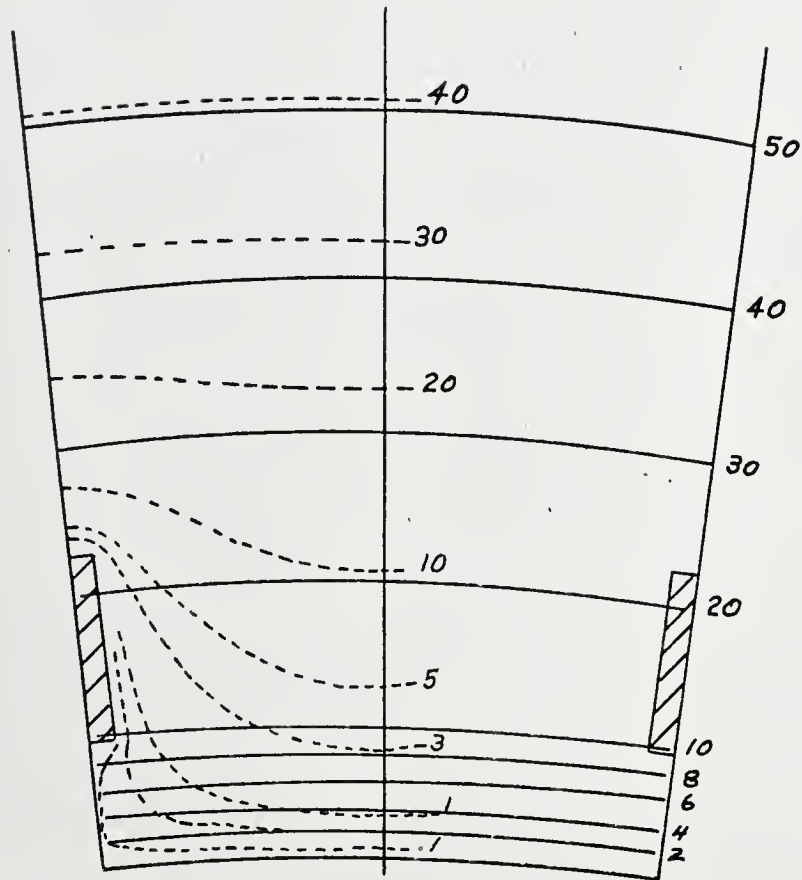


Figure B-1. Single Cell Electrolytic Tank Equipotential Plot

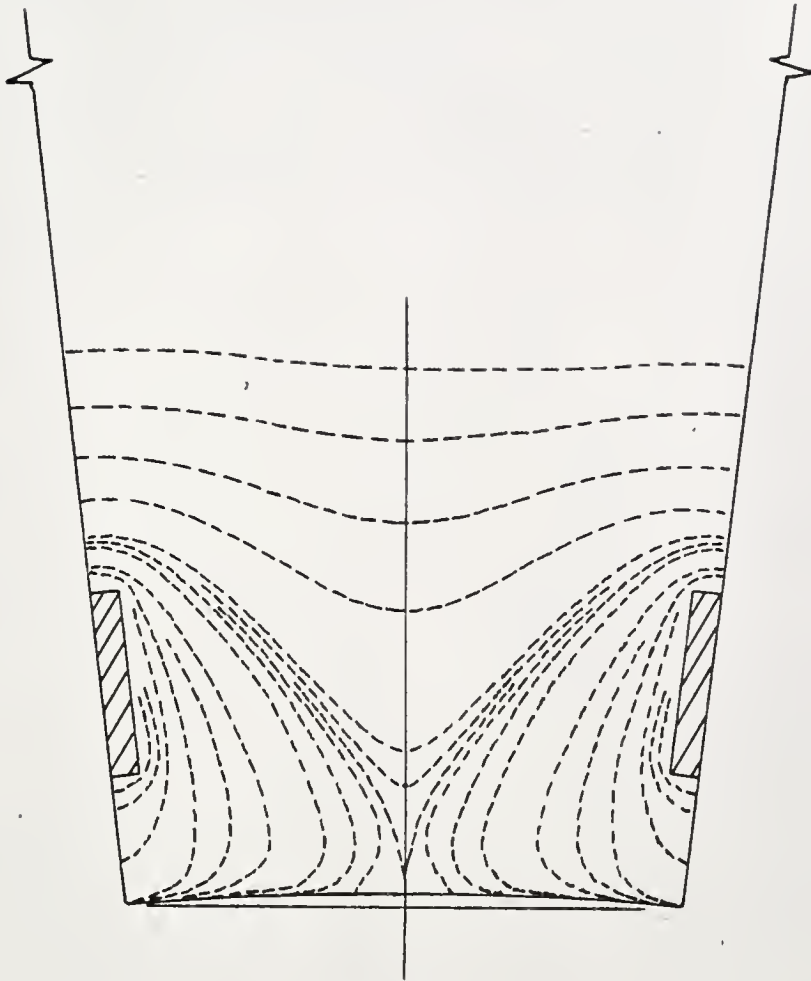
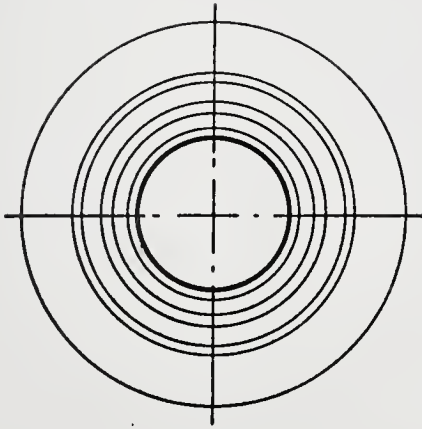
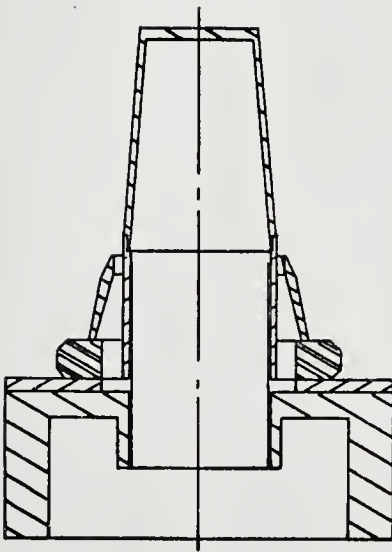


Figure B-2. Equipotential Profile at Cut-off.



end
projection



side
view

Figure B-3. Cross-section of a 24 Vane Grid Structure

24 vane grid structure assembled with the cathode support structure. This is a scaled section of the first structure evaluated.

Constant Mu Design

After experimental evaluation of the vane grid structure, it became apparent that an improvement in perveance for the same absolute cut-off μ was possible since cut-off along the cathode was non-uniform.

The height of the grid vanes above the cathode was held constant in the first design. However, since the pitch of the actual conical grid slowly changes, a decrease in height toward the small end of the cathode is necessary to keep a constant μ . The degree of taper required is a function of cone semiangle grid pitch and cathode-anode separation. Cylindrical approximations of the gridded prototype diode were made at both the large and small ends of the cathode. Electrolytic tank evaluation of each section for a constant μ showed that a 33% vane height taper was required. Theoretically, this reduced height at the exit end of the cathode should also reduce beam perturbations.

Helical Grid Design

The design objective was to construct a simulation of the grid ring structure discussed in Chapter II. Since support and electrical isolation of such a structure requires protruding support posts through the cathode (a most impractical design), a supported helical structure was substituted. A schematic of the completed grid structure mounted to the focus electrode is shown in Figure B-4. To minimize the perturbations and the projected grid-cathode mask ratio, the grid vane size was reduced to a .004 x .007 inch cross-section. The grid pitch was held constant at .050 inches. The four support struts were spot-welded to each turn of the grid.

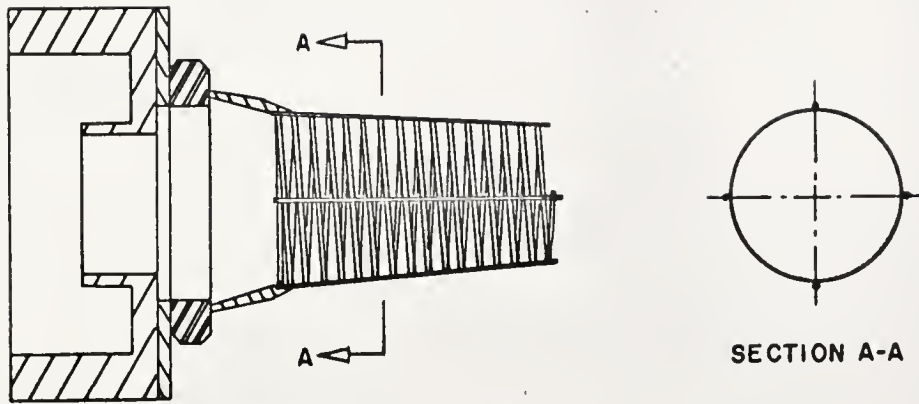


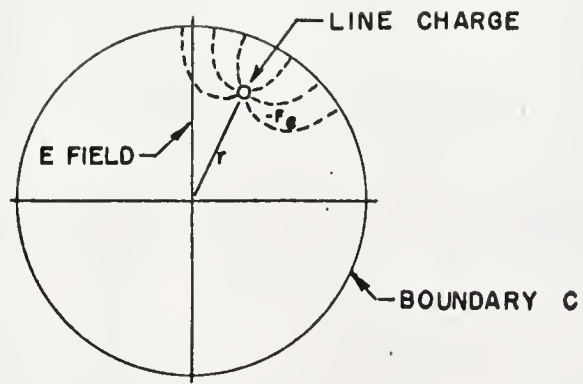
Figure B-4. Helical Grid Structure

APPENDIX C

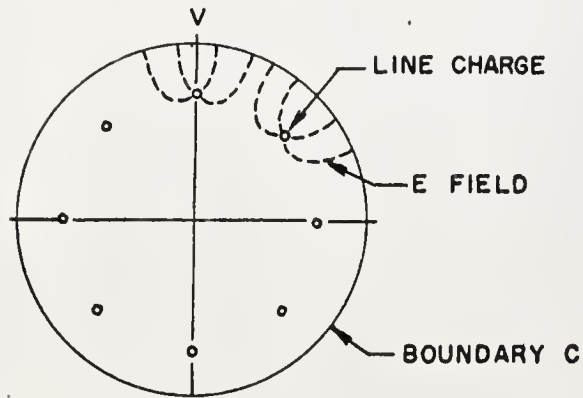
DERIVATION OF THE ELECTROSTATIC POTENTIAL DISTRIBUTION FOR AN ARRAY OF LINE CHARGES LOCATED INSIDE A CYLINDRICAL CONDUCTING BOUNDARY

General

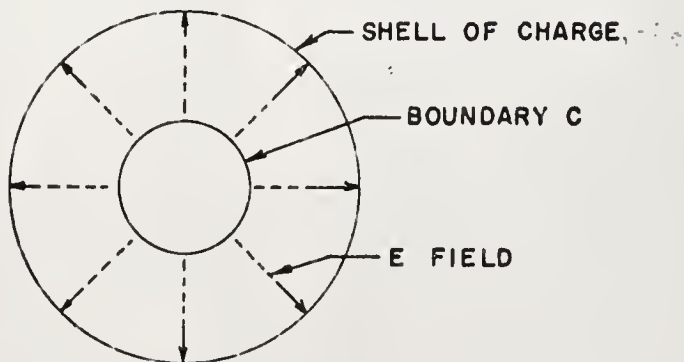
The derivation in this section serves to augment the analysis of beam dynamics discussed in Chapter II. Figure C-1 shows the sequence for reducing a single line charge located off axis but parallel to the symmetry axis of a conducting cylinder, C , to a shell of charge concentric with the cylinder. Now consider n line charges spaced $\frac{2\pi}{n}$ radians apart. As n approaches infinity, the array becomes a hollow cylindrical shell of charges having the same axis of symmetry as the conducting boundary. The authors Brewer [14], Wang [19] and Dow [20] have discussed this type concentric arrangement with application to hollow beams. For the hollow beam case, there are no variations of electric field with the θ component of an (r, θ, z) cylindrical coordinate system. Further, it is



a.



b.



c.

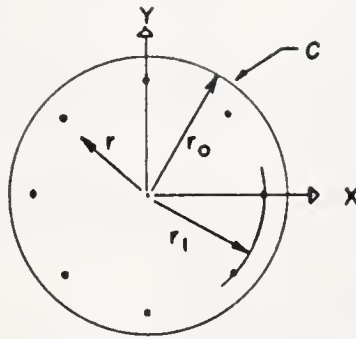
Figure C-1. Sequence of Reducing a Line Charge Located off Axis to Standard Form

usually possible in electron beam problems to neglect variations in the axial, z , direction leaving only the radial coordinate, r , in the electric field solution.

Derivation

Consider a finite number of line charges, n , periodically spaced $\frac{2\pi}{n}$ radians apart. This system is not axial symmetric since the electric field is periodic in θ ; thus, the potential, ϕ , associated with the system will be a function of both r and θ . Variations of ϕ with z are small and will be assumed zero in this derivation. Figure C-2a shows an arrangement of line charges for $n = 8$. In this plane, which will be referred to as the Z -plane, a solution to Laplace's equation is quite difficult. The problem can be simplified through successive conformal transformations (see Churchill [21]) to a plane in which Laplace's equation can be solved from obvious symmetries such as a line charge or shell of charge located concentric with the axis of symmetry.

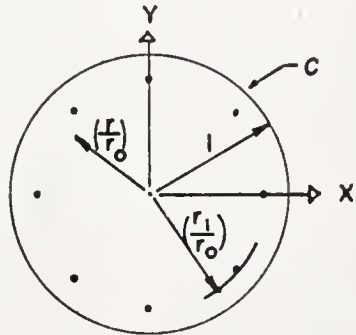
The array of Figure C-2a can be transformed to the single line charge of Figure C-2b by the following transformation:

Z PLANE

C-2a

Z' PLANE

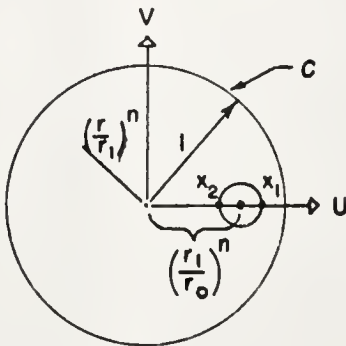
$$z' = \frac{|z| e^{j\theta}}{r_0}$$



C-2b

W PLANE

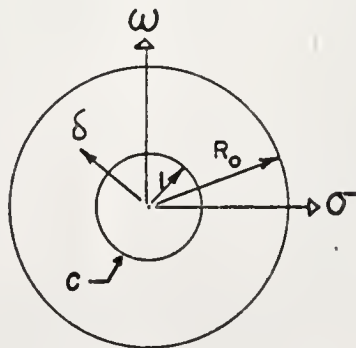
$$w = (z')^n$$



C-2c

P PLANE

$$p = \frac{w-a}{aw-1}$$



C-2d

Figure C-2. Conformal Transformations

$$\left. \begin{aligned} Z' &= \frac{Z}{r_0} \\ W &= (Z')^n \end{aligned} \right\} \quad (C-1)$$

where

$$Z = x + jy$$

$$W = u + jv$$

This configuration can be transformed to the concentric arrangement of Figure C-2d through the bilinear transformation

$$P = \frac{W - a}{aW - 1} \quad (C-2)$$

These transformations are summarized in Figure C-2.

Symbols defined in Figure C-2 will be used in the following derivation.

The first step is to normalize the variables in the Z-plane by

$$Z' = \frac{Z}{r_0} = \frac{|Z|}{r_0} e^{j\theta} = \frac{r}{r_0} e^{j\theta} \quad (C-3)$$

The boundary, C , in the Z-plane becomes a unit circle in the Z'-plane and will transform to a unit circle in the W-plane. Using the transformation,

$$W = (Z')^n = \left(\frac{r}{r_0}\right)^n e^{jn\theta} \quad (C-4)$$

the P-plane representation becomes

$$P = \frac{\left(\frac{r}{r_0}\right)^n e^{jn\theta} - a}{a\left(\frac{r}{r_0}\right)^n - 1} \quad (C-5)$$

where

$$a = \frac{1 + x_1 x_2 + \sqrt{(1 - x_1^2)(1 - x_2^2)}}{x_1 + x_2} \quad (C-6)$$

and

$$R_0 = \frac{1 - x_1 x_2 + \sqrt{(1 - x_1^2)(1 - x_2^2)}}{x_1 - x_2} \quad (C-7)$$

These expressions apply for $a > 1$ and $R_0 > 1$ when $-1 < x_2 < x_1 < 1$. In the P-plane, the boundary, C, of the Z-plane becomes a unit circle concentric with a shell of charge at radius, R_0 . Since the original line charges are negative, the surface charge on the conducting cylinder in the P-plane will be $+q_\ell$ uniformly distributed around C. In this plane, the electric field is radial, as illustrated in Figure C-2d. From Gauss' law, the electric field can be calculated for radius, δ , as

$$\int_S \bar{D} \cdot \overline{da} = \text{charge enclosed} = +q_\ell \quad \delta > 1 \quad (C-8)$$

where \bar{D} is the electric flux density vector and \overline{da} is the incremental surface area of surface, c.

Since

$$D_r = \epsilon E_r = -\epsilon \nabla \Phi = -\epsilon \frac{\partial \Phi}{\partial \delta} \quad (C-9)$$

and

$$da = 2\pi \delta L \quad (C-10)$$

where L is the cylinder length and ϵ is the permittivity.

Then

$$-2\pi\delta L\epsilon \frac{\partial\Phi}{\partial\delta} = +q_\ell \quad (C-11)$$

Taking $L = 1$ and q_ℓ as the charge per unit length

$$\frac{\partial\Phi}{\partial\delta} = \frac{-q_\ell}{2\pi\delta\epsilon} \quad (C-12)$$

Therefore

$$\Phi = \frac{-q_\ell}{2\pi\epsilon} \ln\delta + c_1 \quad (C-13)$$

c_1 is the constant of integration and can be evaluated from the boundary conditions. Taking the unit cylinder as the zero reference potential, c_1 becomes

$$c_1 = \frac{+q_\ell}{2\pi\epsilon} \ln(1) = 0 \quad (C-14)$$

Φ in the P-plane becomes

$$\Phi_p = \frac{-q_\ell}{2\pi\epsilon} \ln\delta \quad \text{for } \delta \geq 1 \quad (C-15)$$

The potential can now be expressed in the original Z-plane by expressing δ in terms of the original coordinates. Using Equation (C-2)

$$P = \frac{\left(\frac{r}{r_0}\right)^n e^{jn\theta} - a}{a\left(\frac{r}{r_0}\right)^n - 1} \quad (C-16)$$

Since

$$P = \sigma + j\omega = \delta e^{j\psi}$$

and δ is the only coordinate in Equation (C-15), the potential in the Z-plane can be written as

$$\Phi_z = \frac{-q\ell}{2\pi\epsilon} \ln \left| \frac{\left(\frac{r}{r_0}\right)^n e^{jn\theta} - a}{a\left(\frac{r}{r_0}\right)^n e^{jn\theta} - 1} \right| \quad (C-17)$$

Solving for the magnitude of the logarithmic term, the numerator becomes

$$\begin{aligned} \left| \left(\frac{r}{r_0}\right)^n e^{jn\theta} - a \right| &= \left(\left(\frac{r}{r_0}\right)^n \cos n\theta - a + j\left(\frac{r}{r_0}\right)^n \sin n\theta \right) \\ &= \left[\left(\frac{r}{r_0}\right)^{2n} \cos^2 n\theta - 2a\left(\frac{r}{r_0}\right)^n \cos n\theta + \left(\frac{r}{r_0}\right)^{2n} \sin^2 n\theta \right. \\ &\quad \left. + a^2 \right]^{1/2} \\ &= \left[\left(\frac{r}{r_0}\right)^{2n} - 2a\left(\frac{r}{r_0}\right)^n \cos n\theta + a^2 \right]^{1/2} \quad (C-18) \end{aligned}$$

Likewise, the denominator becomes

$$\begin{aligned} a\left(\frac{r}{r_0}\right)^n e^{jn\theta} - 1 &= \left[a^2 \left(\frac{r}{r_0}\right)^{2n} \right. \\ &\quad \left. - 2a\left(\frac{r}{r_0}\right)^n \cos n\theta + 1 \right]^{1/2} \quad (C-19) \end{aligned}$$

Therefore

$$\Phi_z = \frac{-q\ell}{2\pi\epsilon} \ln \left[\frac{\left(\frac{r}{r_0}\right)^{2n} - 2a\left(\frac{r}{r_0}\right)^n \cos n\theta + a^2}{a^2 \left(\frac{r}{r_0}\right)^{2n} - 2a\left(\frac{r}{r_0}\right)^n \cos n\theta + 1} \right]^{1/2} \quad (C-20)$$

With line charges of infinitesimal radius, $x_1 = x_2$.

The value of a for this case is $\frac{1}{x_1}$. The location of the center of the line charge in the W-plane is x_1 ,

which represents a distance $\left(\frac{r_1}{r_0}\right)^n$. Substituting

$a = \left(\frac{r_0}{r_1}\right)^n$ into (C-20) yields

$$\Phi_z = \frac{-q\ell}{4\pi\epsilon} \ln \left[\frac{\left(\frac{r}{r_0}\right)^{2n} - 2\left(\frac{r}{r_1}\right)^n \cos n\theta + \left(\frac{r_0}{r_1}\right)^{2n}}{\left(\frac{r}{r_1}\right)^{2n} - 2\left(\frac{r}{r_1}\right)^n \cos n\theta + 1} \right] \quad (\text{C-21})$$

Check of Boundary Conditions

Substituting $r = r_0$ into (C-21) gives

$$\Phi_z = \frac{-q\ell}{4\pi\epsilon} \ln(1) \quad (\text{C-22})$$

therefore

$$\Phi_z = 0 \quad \text{on the boundary as required.}$$

Substituting $r = r_1$ and $\theta = \frac{2\pi}{n}$ into (C-21) produces a pole at the location of each line charge.

It is noted also that when r goes to zero, the potential remains finite but the gradient of the field goes to zero. Therefore, the axis of the system is a saddle point of electric field.

LIST OF REFERENCES

1. Pierce, J. R., Theory and Design of Electron Beams, D. Van Nostrand, New York, 1954.
2. Ashley, J. R., Sutherland, A. D., and Kolb, W. P., "Pierce Electron Guns with High Mu, Non-Intercepting Current Control Grids," Proc. 5th International Congress on Microwave Tubes, Paris, September, 1964.
3. Kirstein, P. T., and Kino, G. S., "Solutions to the Equations of Space-Charge Flow by the Method of Separation of Variables," Journal of Applied Physics, Vol. 29, No. 12, December, 1958.
4. Kirstein, P. T., "Some Solutions to the Equations of Steady Space-Charge Flow in Magnetic Fields," Journal of Electronics and Control, Vol. 7, pp. 417-422, November, 1959.
5. Waters, W. E., "Magnetron Guns--An Exact Theoretical Treatment," Diamond Ordnance Fuse Labs., Washington, D. C., Report No. TR-843, April, 1960.
6. Waters, W. E., "A Theory of Magnetron Injection Guns," IEEE Trans. on Electron Devices, Vol. ED-10, pp. 226-234, July, 1963.
7. Dryden, V. W., "Exact Solutions for Space-Charge Flow in Spherical Coordinates with Application to Magnetron Injection Guns," Journal of Applied Physics, Vol. 33, No. 10, pp. 3118-3124, October, 1962.

8. Dryden, V. W., "Space-Charge Flow in Spherical Coordinates with Applications to Magnetron-Type Guns," Proc. 4th International Congress on Microwave Tubes, pp. 587-594, September, 1962.
9. Harker, K. J., "Determination of Electrode Shapes for Axially Symmetric Electron Guns," Journal of Applied Physics, Vol. 31, pp. 2165-2170, December, 1960.
10. Harker, K. J., "Electrode Design for Axially Symmetric Electron Guns," Journal of Applied Physics, Vol. 33, pp. 1861-1863, May, 1962.
11. Kino, G. S. and Taylor, N. J., "The Design and Performance of a Magnetron-Injection Gun," IRE Trans. on Electron Devices, Vol. ED-9, pp. 1-11, January, 1962.
12. Okoshi, T., "An Improved Design Theory of a Magnetron Injection Gun," IEEE Trans. on Electron Devices, Vol. ED-11, pp. 349-356, July, 1964.
13. Erickson, E. E. and Sutherland, A. D., "Analysis of Non-Laminar Space-Charge Flow," Proc. 4th International Congress on Microwave Tubes, The Hague, Netherlands, September, 1962.
14. Brewer, G. R., "Some Characteristics of a Cylindrical Electron Stream in Immersed Flow," IRE Trans. on Electron Devices, Vol. ED-4, pp. 134-140, April, 1957.
15. Litton Electron Tube Corporation, Report #3, "High Perveance Gun Study," Contract #DA 36-039-SC-87313, December, 1961.
16. Vaidya, N. C. and Gandhi, O. P., "Performance of Magnetically Compressed O-Type Electron Beams Emitted from Non-Shielded Cathodes," IEEE Trans. on Electron Devices, Vol. ED-13, pp. 453-458, May, 1966.

17. Kyhl, R. L. and Webster, H. F., "Breakup of Hollow Cylindrical Electron Beams," IRE Trans. on Electron Devices, Vol. ED-3, pp. 172-183, October, 1956.
18. Pierce, J. R., Traveling Wave Tubes, D. Van Nostrand, New York, 1950.
19. Wang, C. C., "Electron Beams in Axially-Symmetrical Electric and Magnetic Fields," Proc. IRE, Vol. 38, pp. 135-147, February, 1950.
20. Dow, W. G., "Non-Uniform DC Electron Flow in Magnetically-Focused Cylindrical Beams," Advances in Electronics and Electron Physics, Academic Press, Inc., New York, New York, pp. 2-70, 1958.
21. Churchill, R. V., Introduction to Complex Variables and Applications, McGraw-Hill, New York, 1948.

BIOGRAPHICAL SKETCH

Furnie Smith Bryant, Jr. was born July 11, 1930 at Nichols, South Carolins. He was graduated from Nichols High School in June, 1947, and The Citadel, Charleston, South Carolina, in June, 1952, with a Bachelor of Electrical Engineering degree. While at The Citadel, he was awarded "Gold Stars" for academic achievement, and the Distinguished Military Graduate Award. He entered the Army Ordnance in July, 1952, and served until April, 1956. While in service, he was graduated from Army Ordnance Fire Control School, Aberdeen Proving Ground, Redstone Arsenal Provisional Institute, Guided Missile School, Huntsville, Alabama, and Nuclear Supervisor's School, Albuquerque, New Mexico. He attended the Oak Ridge Institute of Nuclear Studies in 1956, and the summer quarter at Georgia Tech, in the School of Engineering. He joined the staff at Deering-Milliken Research Corporation in September, 1956, and worked in the field of utlrasonics. He joined the

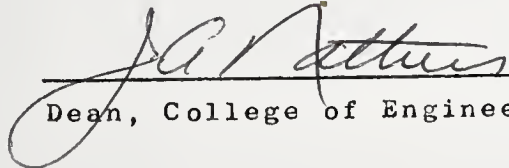
Clemson University Department of Electrical Engineering Staff in February, 1957, and there received the degree of Master of Science in Engineering in February, 1959. He joined the Research and Development Staff of Sperry Electronic Tube Division in Gainesville, Florida, in June, 1959, and began work toward the degree of Doctor of Philosophy.

While at Sperry he has served as Project Engineer for the design and construction of traveling wave tubes and backward wave oscillators. He was made a Senior Engineer in the Research Department in 1964, and since then he has been primarily engaged in a negative grid crossed-field electron gun investigation sponsored by the Sperry Electronic Tube Division, which was the basis for his dissertation.

Furnie Smith Bryant, Jr. is married to the former Rosa Platt and has two daughters. He is a member of the Institute of Electrical and Electronics Engineers, Professional Group on Electron Devices, Professional Group on Microwave Theory and Techniques, National Society of Professional Engineers and Registered Professional Engineer in South Carolina and Florida.

This dissertation was prepared under the direction of the chairman of the candidate's supervisory committee and has been approved by all members of that committee. It was submitted to the Dean of the College of Engineering and to the Graduate Council, and was approved as partial fulfillment of the requirements for the degree of Doctor of Philosophy.


August, 1966




Dean, College of Engineering

Dean, Graduate School

Supervisory Committee:



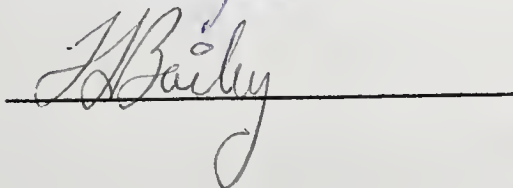
Chairman



Co-Chairman







1 6576-20